Mean Circulation of the Hamburg LSG OGCM and Its Sensitivity to the Thermohaline Surface Forcing

ERNST MAIER-REIMER, UWE MIKOLAJEWICZ, AND KLAUS HASSELMANN

Max-Planck-Institut für Meteorologie, Hamburg, Germany

(Manuscript received 23 July 1991, in final form 26 June 1992)

ABSTRACT

The sensitivity of the global ocean circulation to changes in surface heat flux forcing is studied using the Hamburg Large Scale Geostrophic (LSG) ocean circulation model. The simulated mean ocean circulation for appropriately chosen surface forcing fields reproduces the principal water mass properties, residence times, and large-scale transport properties of the observed ocean circulation quite realistically within the constraints of the model resolution. However, rather minor changes in the formulation of the high-latitude air–sea heat flux can produce dramatic changes in the structure of the ocean circulation. These strongly affect the deep-ocean overturning rates and residence times, the oceanic heat transport, and the rate of oceanic uptake of CO_2.

The sensitivity is largely controlled by the mechanism of deep-water formation in high latitudes. The experiments support similar findings by other authors on the sensitivity of the ocean circulation to changes in the freshwater flux and are consistent with the existence of multiequilibria circulation states with a relatively low transition threshold.

1. Introduction

The oceans play a major role in the dynamics of climate through their large capacity for the transport and storage of heat, moisture, and CO_2. The oceans are driven by the atmosphere, and their response to changes in atmospheric forcing represents one of the most important coupling links within the complex system of climatic feedbacks. The ocean–atmosphere coupling has a strong impact both on the response characteristics of the climate system to external forcing and on internal natural climatic variability.

In addition to these general considerations, there is mounting evidence that the global ocean circulation is a highly sensitive component of the climate system, which can be rather easily driven from one circulation regime to another. The suggestion that the global ocean circulation may exhibit more than one distinct mode of circulation has long been the subject of speculation. Geological evidence indicates that during some periods in the Tertiary, the deep ocean was some 10 degrees warmer and more saline than today, suggesting that in those times deep water was formed by an evaporation–salinity pump operating at relatively low latitudes, for example, in the Mediterranean rather than by cooling and freezing in high latitudes, as in today's ocean (Chamberlin 1906). Stommel (1961) and Rooth (1982) have suggested that even for the same boundary conditions, the ocean circulation may have two distinct steady-state solutions. This conjecture has been supported by numerical experiments with an ocean general circulation model (OGCM) with idealized geometry by Bryan (1986) and by coupled ocean–atmosphere general circulation model experiments by Manabe and Stouffer (1989). The mechanism of such multiple equilibrium states has been investigated in more detail by Welander (1986) and Marotzke et al. (1988).

The sensitivity of the ocean circulation as evidenced by multiequilibria states is borne out also by the strong response of the ocean circulation to small changes in external forcing. It has been conjectured, for example, by Berger and Killingley (1982) and Broecker et al. (1988) that the sudden return of glacial conditions during the Younger Dryas interruption of the holocene warming was due to a transition in the ocean circulation regime triggered by the meltwater runoff from the Laurentide ice sheet. This hypothesis has found support through numerical experiments with the Hamburg Ocean General Circulation Model (Maier-Reimer and Mikolajewicz 1989). Although advanced techniques of dating now seem to rule out the meltwater hypothesis as an explanation specifically of the Younger Dryas (Berger 1990), Sarnthein and Tiedemann (1990) have recently identified several cooling events within the last glacial cycle that appear consistent with the meltwater mechanism.

Smaller climatic fluctuations, such as the warming around A.D. 1000 and the Little Ice Age between the sixteenth and eighteenth century, may also have been caused by internal variations of the coupled global

Corresponding author address: Ernst Maier-Reimer, Max-Planck-Institut für Meteorologie, Bundesstraß 55, D-2000 Hamburg, 13 Germany.

© 1993 American Meteorological Society

ocean–atmosphere circulation system. This view has found support in numerical experiments in which an OGCM was driven by white noise atmospheric forcing (Mikolajewicz and Maier-Reimer 1990).

Further interest in the stability of the ocean circulation has been stimulated by the recent discovery of significant variations in past atmospheric CO_2 concentrations inferred from the analysis of air bubbles trapped in ice cores. A strong correlation has been found between these variations and the observed climate change during the last 160 000 years (Jouzel et al. 1987). Since the oceans represent by far the largest active carbon reservoir in the carbon cycle, most attempts to explain these observations have hypothesized some mechanism for changing the carbon stored in the ocean (cf. review by Berger and Keir 1984). An obvious possible mechanism is the change in the ocean biological pump and deep-ocean carbon storage resulting from a change in the ocean circulation. Recent numerical experiments using a global carbon cycle based on the Hamburg Global Ocean Circulation Model (Maier-Reimer and Hasselmann 1987; Bacastow and Maier-Reimer 1990) indicate that this process is indeed a promising candidate for explaining most, although probably not all, of the observed changes in the carbon system during the last 160 000 years (Heinze et al. 1991). The effectiveness of the process, however, again depends critically on the sensitivity of the ocean circulation to changes in the surface forcing associated with the assumed climatic variations.

In this paper, we use the Hamburg Large Scale Geostrophic (LSG) Global Ocean Circulation Model to investigate the response of the ocean circulation to various modifications in the mean annual (climatological) surface forcing. The ocean circulation is computed for a number of alternative formulations of the surface boundary conditions. All of these may be regarded as acceptable representations of present climatological surface conditions, within the uncertainty of the observations, yet the differences in the simulated circulation patterns are dramatic, particularly in the abyssal ocean. The main source of this sensitivity lies in the formation of deep water at high latitudes, which depends critically on the heat exchange with the atmosphere.

The Hamburg LSG model does not resolve eddies. Reservations have frequently been expressed regarding the applicability of non-eddy-resolving ocean circulation models. We believe these reservations have sometimes been exaggerated. Since their inception in the late 1960s, global ocean circulation models have been reasonably successful in reproducing many of the qualitative features of the global ocean circulation (Bryan 1969; Bryan and Lewis 1979). Moreover, inversion methods based on essentially the same non-eddy-resolving physics as these models have been successfully applied to reconstruct realistic velocity fields from hydrographic and tracer data (Roemmich and Wunsch 1985; Olbers et al. 1985).

The early global ocean circulation models nevertheless suffered from certain basic shortcomings, such as a too deep main thermocline (typically by a factor of order 2) and a slow warming of the deep ocean. These have tended to restrict the application of the models in the fully prognostic thermodynamics mode, leading, for example, to the introduction of the semiprognostic "robust diagnostic" technique for long integrations (Sarmiento and Bryan 1982). However, most of these shortcomings have been largely overcome today through the use of improved numerical methods and a more realistic treatment of diffusion (Redi 1982). Apart from the western boundary currents and their immediate recirculation regimes (which cannot be adequately resolved by present global ocean models, independent of the role of eddies in these regions), the principal features of the observed global ocean circulation, including the main thermocline and deep-ocean circulation, are reproduced realistically by, for example, the Hamburg non-eddy-resolving global circulation model.

The version of the model used in this paper has 11 vertical layers and a horizontal resolution of 3.5° × 3.5° on an E grid (Arakawa and Lamb 1977), with realistic bottom topography and coastlines. An implicit time integration method is used, permitting a long time step of one month. The model has been applied recently in a number of ocean circulation studies (cf. Mikolajewicz et al. 1990; Maier-Reimer et al. 1990a) and has been coupled with the Hamburg atmospheric climate model (Bakan et al. 1991; Cubasch et al. 1992). It has also provided the circulation field for the Hamburg carbon cycle model (Heinze et al. 1991; Maier-Reimer and Bacastow 1990b; and other papers cited above).

A general description of the model (which has not been presented in detail in these previous papers) is given in section 2. Further technical details can be found in the appendixes (on mode decomposition, mode dispersion properties, and numerical diffusion) and in Maier-Reimer and Mikolajewicz (1990). Section 3 describes the mean ocean circulation of the "standard" run. This corresponds to a choice of climatological surface boundary conditions that yielded the closest agreement with the observed circulation. The general structure of the simulated ocean circulation is analyzed with respect to currents, transports, and water mass properties, including apparent radiocarbon age and tracer concentrations. The ocean circulation solutions obtained with alternative formulations of the climatological surface boundary conditions are presented in section 4. The last, section 5 summarizes the principal conclusions of the paper.

2. The global ocean circulation model

The Hamburg LSG Ocean Circulation Model has evolved from an original concept of Hasselmann (1982). This was based on the observation that for a

large-scale ocean circulation model designed for climate studies, the relevant characteristic spatial scales are large compared with the internal Rossby radius throughout most of the ocean, while the characteristic time scales are large compared with the periods of gravity modes and barotropic Rossby wave modes. Under these scaling conditions, the baroclinic velocity field can be determined diagnostically from the given density field through local geostrophy. The barotropic velocity field and surface elevation can also be determined diagnostically for a given density field as the equilibrium barotropic response to the prescribed surface-stress forcing and bottom torque. The only prognostic equations are thus the remaining advection equations for temperature and salinity (for a linearized equation of state, these are identical in the assumed scaling limit to the potential vorticity equation). The approximation breaks down at the equator and in boundary current regions, where it was proposed that the global model should be coupled with appropriate regional models.

By filtering out in this manner the irrelevant fast modes, retaining only the slow modes represented by the prognostic temperature and salinity equations, Hasselmann estimated that a relatively long time step of one month could be achieved, as compared with a few hours for explicit primitive equation models. It was found in practice, however, that a straightforward numerical implementation of these concepts led to various numerical instability problems, particularly in the treatment of the interactions with the bottom topography.

Accordingly, in the present version of the model, the fast modes have been filtered out by the more conventional technique of integrating the complete set of primitive equations, including all terms except the nonlinear advection of momentum, by an implicit time integration method. The free surface is also treated prognostically, without invoking a rigid-lid approximation. The numerical scheme is unconditionally stable and has the additional advantage that it can be applied uniformly to the entire globe, including the equatorial and coastal current regions. The simulations presented in this paper were carried out with a one-month time step.

Applying the standard hydrostatic and the Boussinesq approximations and neglecting the vertical friction, the prognostic equations of the system (in standard notation) are given by the horizontal momentum equation:

$$u_t - fv + \frac{1}{R\cos\varphi}\frac{p_\lambda}{\rho_0} = \frac{\tilde{\tau}^\lambda}{\rho_0} + A\Delta u \qquad (1)$$

$$v_t + fu + \frac{1}{R}\frac{p_\varphi}{\rho_0} = \frac{\tilde{\tau}^\varphi}{\rho_0} + A\Delta v, \qquad (2)$$

where $\tilde{\tau}$ is the wind stress divided by the thickness of the uppermost model layer, acting only at the surface; the equation for the evolution of the potential temperature ϑ and salinity S:

$$\vartheta_t + \frac{u}{R\cos\varphi}\vartheta_\lambda + \frac{v}{R}\vartheta_\varphi + w\vartheta_z = q^\vartheta + D\Delta\vartheta \qquad (3)$$

$$S_t + \frac{u}{R\cos\varphi}S_\lambda + \frac{v}{R}S_\varphi + wS_z = q^S + D\Delta S, \qquad (4)$$

(the sources q^ϑ and q^S occur only in the surface layer); and the evolution equation for the surface elevation ζ, given by the surface boundary condition,

$$\zeta_t = w \quad \text{at} \quad z = 0. \qquad (5)$$

The prognostic equations are complemented by the diagnostic relations:

continuity,

$$w_z + \frac{1}{R\cos\varphi}((v\cos\varphi)_\varphi + u_\lambda) = 0; \qquad (6)$$

hydrostatic pressure relation,

$$p = g\rho_0\left(\zeta + \frac{1}{\rho_0}\int_z^0 \rho(z')dz'\right); \qquad (7)$$

and the equation of state, for which we use the (UNESCO 1981) formula,

$$\rho = \rho(S, T, p), \qquad (8)$$

in which the in situ temperature T is expressed as a function of p and the potential temperature ϑ. In the experiments described in this paper, we converted ϑ to T using the simplified formula

$$T = \vartheta + \xi z \quad [\xi = 0.12\ \text{K km}^{-1}],$$

corresponding to a linearization of Bryden's (1973) full formula at $T = 2°\text{C}$ and $z = 4$ km.

It is convenient to decompose the velocities in the form

$$u, v = (U + u', V + v'), \qquad (9)$$

where $(U, V) = \int_{-B}^0 (u, v)dz/B$ and u', v' denote the barotropic and baroclinic components of motion, respectively. The baroclinic system is described by equations for the vertical velocity shear, obtained from the difference between two adjacent levels of computation. This corresponds to a decomposition of the N-layer baroclinic system into N-1 two-layer systems, which represent our basic computational modes.

For these shear modes and for the barotropic mode we derive simplified mode equations for $\tilde{u}, \tilde{v}$ that have the same structure as for a single-layer fluid:

$$\tilde{u}_t - f\tilde{v} + p_x = A\Delta u$$

$$\tilde{v}_t + f\tilde{u} + p_y = A\Delta v$$

$$p_t + c^2(\tilde{u}_x + \tilde{v}_y) = 0, \qquad (10)$$

where c^2 arises through the integration over the strat-

ification. The systems are solved by a rigorous Euler–backward method:

$$\tilde{u}^t - f\delta t\tilde{v}^t + \delta t p_x^t - \delta t A\Delta\tilde{u}^t = \tilde{u}^{t-\delta t} \quad (11a)$$

$$\tilde{v}^t + f\delta t\tilde{u}^t + \delta t p_y^t - \delta t A\Delta\tilde{v}^t = \tilde{v}^{t-\delta t} \quad (11b)$$

$$p^t + \delta t c^2(\tilde{u}_x^t + \tilde{v}_y^t) = p^{t-\delta t}. \quad (11c)$$

By insertion of (11c) into (11a) and (11b), we obtain a simultaneous elliptic system for u^t and v^t. For the baroclinic modes the system can be easily solved by iteration. For the barotropic system, however, the iterative procedure was found to converge too slowly and a solution by direct elimination was therefore used. The time consuming step of triangularization needs to be carried out only a few times, since the basic stratification does not change substantially as one approaches stationarity.

The advection of temperature and salinity is computed by an upwind discretization method, which is implicit in time. Upwind schemes have a high inherent numerical diffusivity. On the other hand, centered difference schemes need, due to their bad dispersion properties, higher explicit diffusion terms in order to suppress negative sidelobes, which do not arise in first-order schemes. The required additional diffusivity is generally of the same order as the implicit numerical diffusivity of the first-order scheme. In practice, we found that the numerical diffusion of our scheme was tolerable and if anything, slightly smaller (as evidenced, for example, by the realistic depth of the main thermocline) than the net effective diffusivity incurred with published models of comparable resolution that used centered difference schemes (e.g., Bryan and Lewis 1979). The numerical diffusivity is noticeable mainly in regions of strong currents, where it could be argued that it is, in fact, needed as a parameterization of the nonresolved mixing by baroclinically unstable current fluctuations and eddies.

Convective mixing is introduced whenever the stratification becomes unstable. Stability of a vertically neighboring pair of grid cells is defined by comparing their potential densities computed at their common interface level. We stabilized the water column with the minimal mixing compatible with the conservation of heat and salt. For equally sized grid cells (below 1000 m) this is achieved by complete interchange of water properties. For layers of different thickness the water in the thinner layer is exchanged with an equal volume of water from the thicker layer, and the newly injected water in the thicker layer is then mixed with the residual water of the cell. The mixing algorithm is applied successively to all pairs of layers, beginning from the top. This procedure is performed only once per time step, so that the entire water column does not necessarily become completely stable. However, we found experimentally that a repeated mixing cycle would be activated for only 5% of the convection locations and would release, in these cases, only 1% additional potential energy. In the case of ice formation, the evicted brine is distributed equally over the top two layers. We emphasize that although our mixing procedure appears intuitively reasonable, certain properties of the circulation may depend sensitively on the details of the convection mechanism, as has been pointed out by Marotzke (1991) for a rather different model.

The horizontal spatial discretization is on an E grid (Arakawa and Lamb 1976). This has some known disadvantages in the representation of short gravity waves, but for the geostrophic modes of interest here it yields simple interpolation-free difference expressions for the relevant spatial derivatives. The E grid is staggered and therefore produces split modes, but mode divergence is suppressed by moderate viscosity and diffusion terms (5×10^4 and 2×10^2 m^2 s^{-1}, respectively).

A general analysis of the dispersion properties of the discretization scheme on the globe has not been attempted. However, some of the principal modifications of wave propagation in midlatitudes and along the equator are discussed in the β-plane approximation in appendix B. The discretization scheme has negligible effect on the propagation of slow internal Rossby waves, in which we are principally interested, but produces a strong damping and retardation of fast free modes, as intended. The quasistationary, forced fast modes, which we also wish to retain, are similarly not significantly distorted.

For the present application, the model was run on two staggered 5° × 5° global grids with 11 vertical levels, yielding an effective grid resolution of 3.5°. Horizontal velocity, temperature, and salinity were specified at depth levels 25, 75, 150, 250, 450, 1000, 2000, 3000, 4000, and 5000 m, (cf. Fig. 1), while vertical velocity and pressure were defined at the intermediate levels. The model includes a realistic smoothed bottom topography.

In this configuration, the model requires approximately 3 seconds per time step on one CRAY 2S processing unit. This is about four times the requirement of a more conventional GCM with explicit discretization schemes (Latif et al. 1993). However, the large time step of one month more than offsets the disadvantage of the more complex numerics and makes the model an order of magnitude more efficient than an equivalent explicit model.

In all simulations the circulation was driven by a given wind stress field (from Hellerman and Rosenstein 1983) and the observed surface-layer salinity field (from Levitus 1982). To smooth the response, the observed salinity values were coupled to the top ocean layer through a linear Newtonian relaxation term with a time constant of typically a few months.

The thermal forcing was similarly computed using a simple Newtonian heat flux relation from a prescribed atmospheric or ocean surface temperature field.

In most experiments, a simple thermodynamic ice model was included. Whenever the heat loss to the atmosphere within a time step leads to an ocean tem-

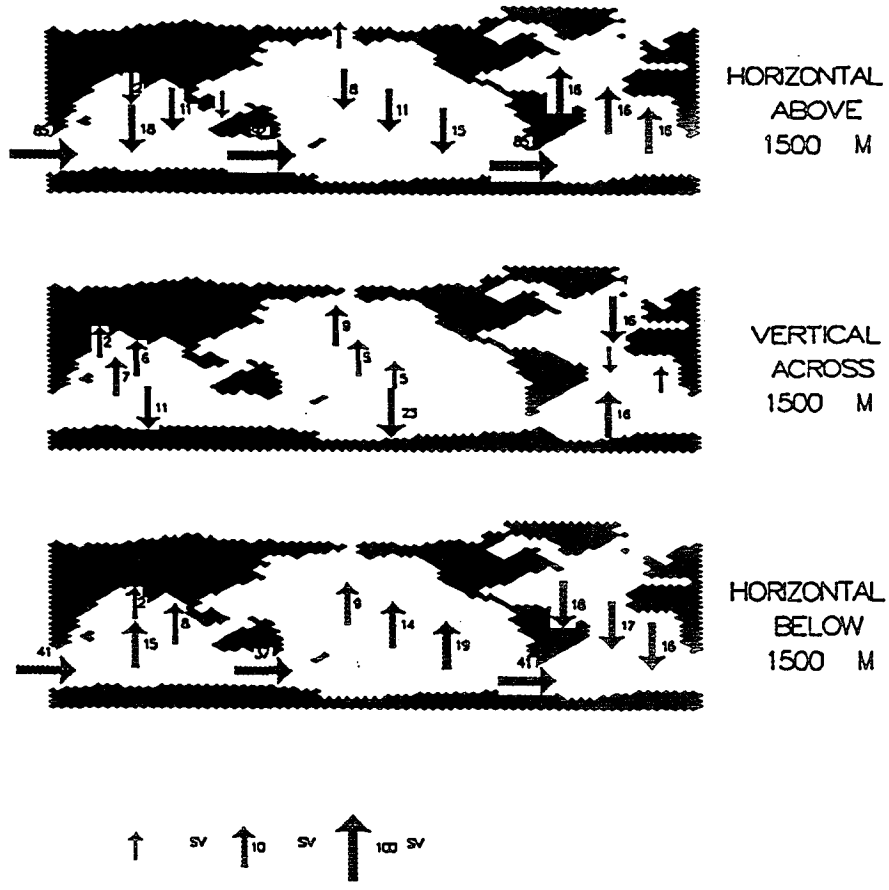

FIG. 1. The conveyor belt circulation of the standard run.

perature below the freezing point T_f, the temperature is held fixed at T_f and the excess heat loss is used to produce sea ice. The heat flux over sea ice can be represented approximately as

$$H = D(T_a - T_f)/h, \tag{12}$$

where h is the ice thickness, D the heat conductivity of ice, and T_a the atmospheric temperature (Stefan 1891). The rate of ice formation is then given by

$$\frac{dh}{dt} = -\frac{H}{E}, \tag{13}$$

where E is the enthalpy of melting, which can be solved to yield

$$h = \sqrt{2D(T_f - T_a)(t - t_0)/E}, \tag{14}$$

where t_0 is the freezing onset time.

The analytical square-root expression (14) applies primarily for the first time step in which sea ice is formed. It yields a better description of ice growth in the initial stages than a straightforward linear finite-difference relation (note that the time derivative of the ice thickness is initially infinite). It also yields a correct partitioning of the heat flux into ocean and ice. A similar difference formula based on the exact integration of Eqs. (12) and (13) is used also as if ice is already present at the onset of a time step.

3. The reference run

For the reference run, the model was driven by the monthly climatological wind stress fields from Hellerman and Rosenstein (1983), by an effective monthly mean air temperature constructed from the COADS dataset (Woodruff et al. 1987) and by the annual-mean surface salinity from Levitus (1982). This was used in all runs [the seasonal dataset of Levitus appeared to be less reliable, perhaps due to the sparseness of the original data.] The Newtonian time constant was taken as two months for both salinity and temperature coupling. The prescribed salinity boundary condition was used to compute an equivalent freshwater flux (rather than an equivalent salinity source, since we wish to conserve salt in our model). The freshwater flux yields a small but nonnegligible additional mass flux source term, which must be included in the computation of sea level.

To determine the effective air temperature, the observed atmospheric surface temperatures from the COADS dataset were combined with the climatological wind field in an advection equation

$$T_{at} + v_i \partial_i T_a = \lambda(T_{\text{COADS}} - T_a). \quad (15)$$

Equation (15) may be regarded as a simple one-layer parameterization of the atmospheric boundary layer. The approach was motivated by the observation that the measured monthly mean atmospheric temperatures, averaged over a grid resolution cell, are normally rather close to thermal equilibrium with the oceans. These climatological mean values are unable to capture the strong heat transfer from the oceans to the atmosphere through short sub-time-scale synoptic processes, such as cold air outbreaks from the continents, cold polar air flows in the afterwake of passing cyclones, etc. A reliable estimate of these contributions would require a detailed statistical analysis of the correlation of the short time-scale fluctuations of air, temperature, and wind speed. As this is difficult to carry out on a global basis, we attempt to parameterize such subscale processes with the simple ingredient of an advection term proportional to the local mean wind velocity. This has the plausible property that it yields the largest contributions where the background mean wind field crosses strong thermal gradients in the ocean (e.g., off continental coasts and near thermal fronts such as the Gulf Stream). In general, the advection corrections are larger in the Northern Hemisphere than in the Southern Hemisphere, where the wind fields and surface ocean currents tend to be more strongly zonally aligned. As discussed in the following section, the introduction of such a sub-grid-scale correction term significantly improved the simulation of North Atlantic deep-water formation and the deep-ocean circulation in general.

The gross transport properties of the global ocean circulation are summarized in Fig. 1, which shows the

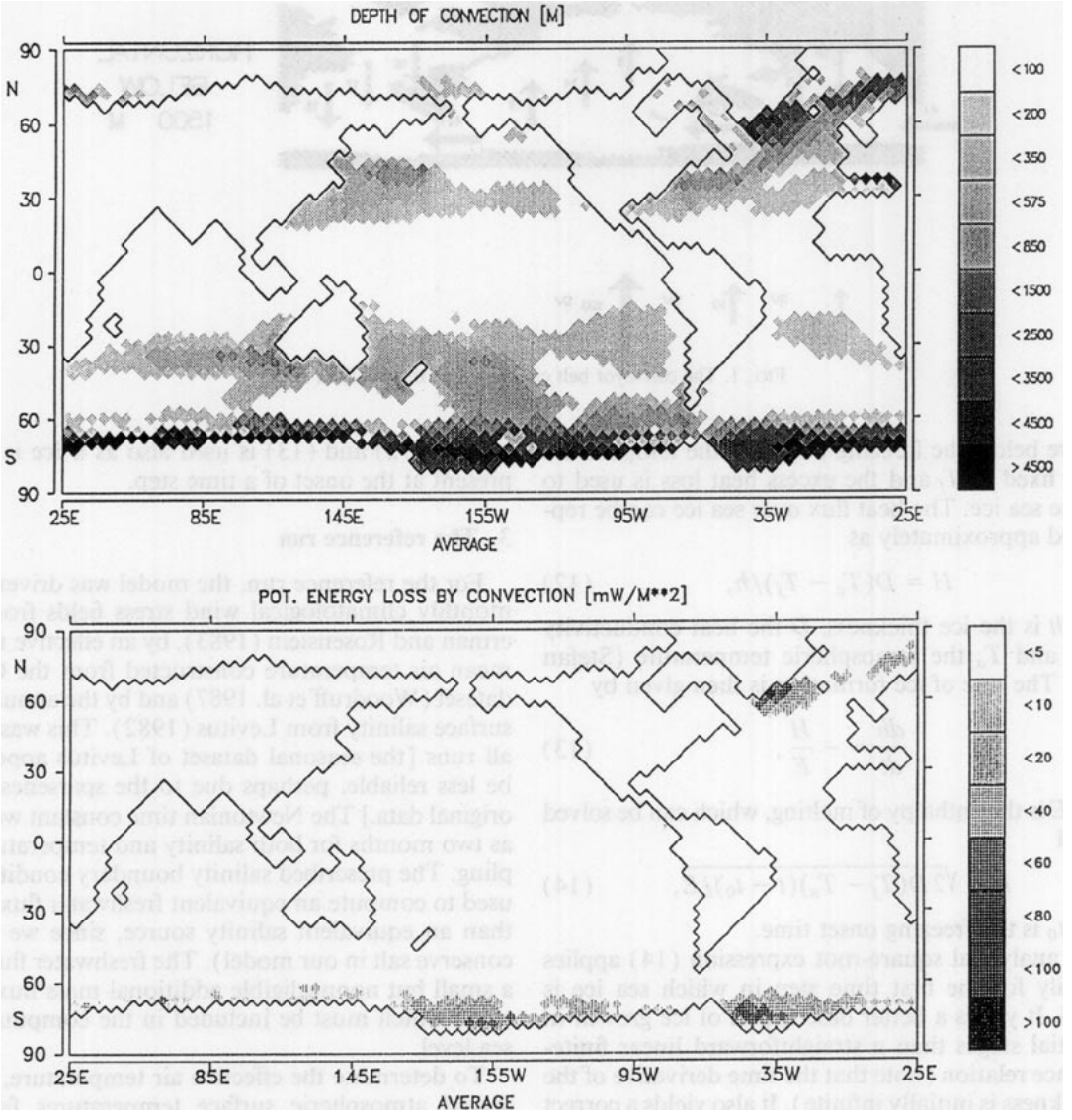

FIG. 2. (a: top) Depth of convective column produced by surface cooling.
(b: bottom) Release of potential energy by convective mixing.

zonally (meridionally in the ACC) integrated net mass fluxes between various characteristic ocean regions. The annual-mean circulation was averaged for this representation over 24 boxes, obtained by dividing the ocean into an upper and lower layer, separated by the 1500-m depth level, and segmenting the layers by latitudinal boundaries at 10°N, 10°S, and 40°S (in addition to the natural meridional ocean basin boundaries). The upper and lower panels of Fig. 1 show the meridional mass fluxes of the three major oceans and the zonal circumpolar flux in the Southern Ocean for the upper and lower layers, respectively. The center panel shows the vertical flux across the 1500-m level interconnecting the two layers.

The basic features of the standard "conveyor belt" picture (Wüst 1933; Gordon 1986) are well reproduced. The main source of deep water is in the northern Atlantic. The deep salty water, formed first in the northern Atlantic, spreads across the equator into the South Atlantic, Indian Ocean, and Pacific, joining the Antarctic Circumpolar Current. The return flow is almost completely through the Drake passage; only 1.5 Sv pass through the narrow Banda Strait between Indonesia and Australia (this feature is very sensitive, however, to the representation of the topography in the Banda Strait, which is not well resolved in the present model). Upwelling occurs mainly in equatorial regions.

Figure 2a shows the depth of the convective column produced by surface cooling (the depth of the convective column is defined as the greatest depth connected with the surface by at least one convection event within an annual cycle). Most of the model ocean is seen to be stably stratified. Deep convection occurs mainly around Antarctica, particularly off the Ross and Weddell ice shelves, and in the North Atlantic where two regions of deep-water production can be seen: the Irminger Sea, southeast of Greenland, where extremely cold air is advected from the Greenland ice sheet, and the Norwegian Sea, where high salinity water of the Gulf Stream system extends into the Arctic basin.

Figure 2a can not be interpreted as a direct measure of the rate of deep-water formation, as it contains no information on the strength of convection. A measure of the intensity of convective overturning is provided by the rate of release of potential energy within the water column, shown in Fig. 2b. The North Atlantic and Weddell Sea deep-water sources are now more evident. The difference between the North Pacific, characterized by stable stratification, and the convective high-latitude regions of the other oceans is also seen more clearly.

Another source of deep-water formation is large-scale subduction, indicated by the zonally averaged meridional overturning circulation (Fig. 3a). In the surface waters, two nearly symmetrical Ekman cells are formed on either side of the equator, while a third surface cell is seen in the Antarctic Circumpolar Current (ACC). The largest deep overturning cell lies in the Southern Ocean. It is driven mainly by dense Weddell Sea water.

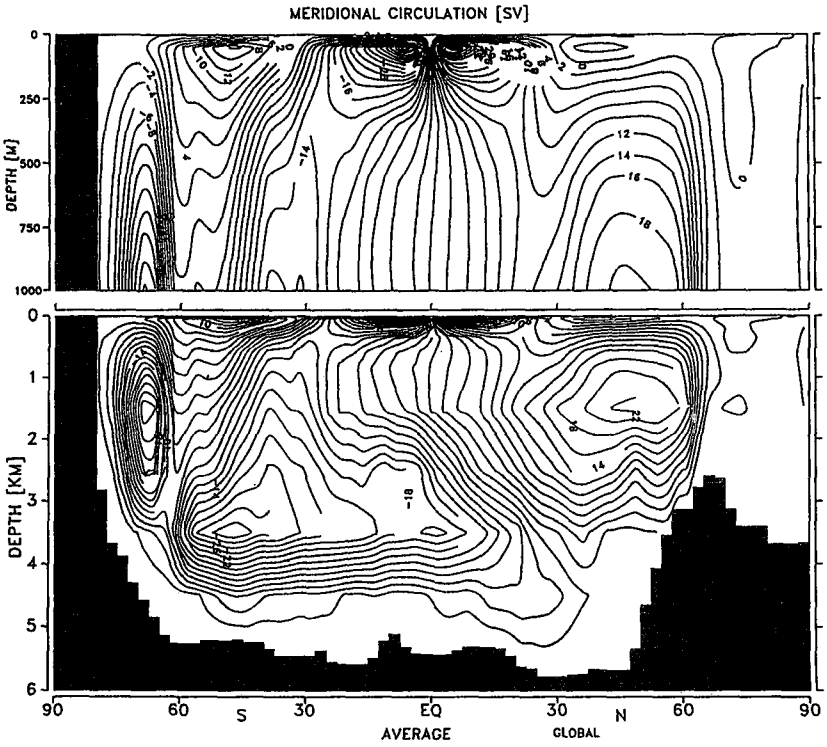

FIG. 3a. Global meridional overturning circulation.

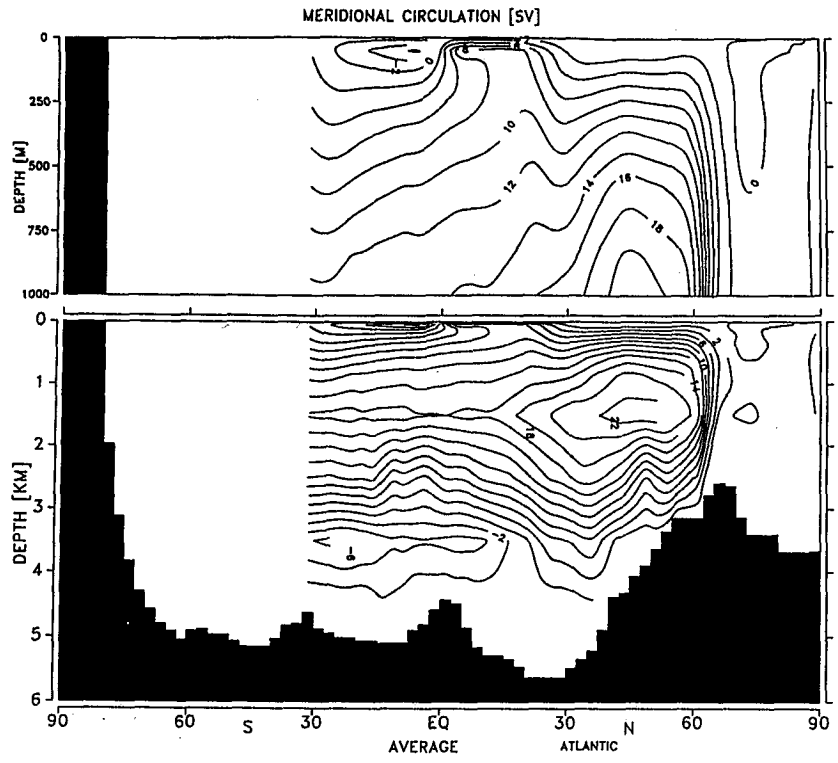

FIG. 3b. Atlantic meridional overturning circulation.

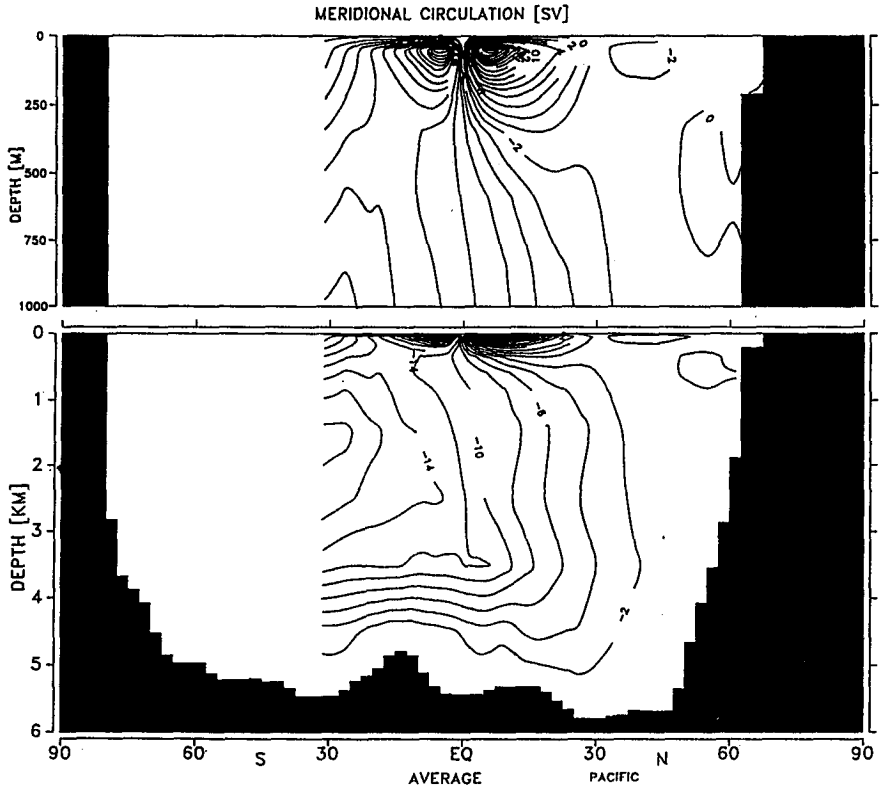

FIG. 3c. Pacific meridional overturning circulation.

However, the overturning cell in the North Atlantic is only slightly smaller, despite the much smaller geographical area of the North Atlantic compared with the full zonal extent of the Southern Ocean.

Figures 3b and 3c show the individual meridional circulation patterns for the Atlantic and Pacific. The difference between the two oceans is pronounced. The tropical Pacific exhibits a rather symmetrical Ekman circulation in the upper kilometer and a deep inflow from the Antarctic sea, which ventilates the North Pacific. The apparent inflow of more than 10 Sv (Sv $\equiv 10^6$ $m^3 s^{-1}$) of deep water into the Ekman cells is partly an artifact of the zonal integration, which includes the strong equatorial upwelling near the Peruvian coast and at the western boundary. This feature, nevertheless, appears inconsistent with the schematic flow diagrams derived from the analyses of tracer fields (Fiadeiro 1982; Wunsch et al. 1983), in which the inflow of AABW is compensated for by a return flow at intermediate depth. The impact of this discrepancy on the tracer distributions, however, seems to be only minor: Fig. 15b compares the GEOSECS section of radiocarbon with the simulation. Apart from an offset of 40 per mille created by the strong mixing around Antarctica, the structures in the Pacific appear to be realistic. The absolute minimum is at 1 km instead of 2 km as in the GEOSECS data—a shift by one computation level in the model. In the Atlantic, the surface Ekman cells are much weaker; the upper kilometer is dominated by the strong inflow from the Southern Ocean. The deep Atlantic is characterized by a strong outflow from the Northern Atlantic and a small bottom inflow from the south.

In comparing flow patterns and tracer distributions it should be kept in mind that the transports shown in Fig. 3 do not represent the total water exchange. A significant fraction of the total exchange occurs through convective mixing and also through vertical motions in limited regions, which are averaged out in the zonal integrations shown in Figs. 3a–c.

Figure 4a shows the annual-mean surface topography, which reflects primarily the vertical integral of

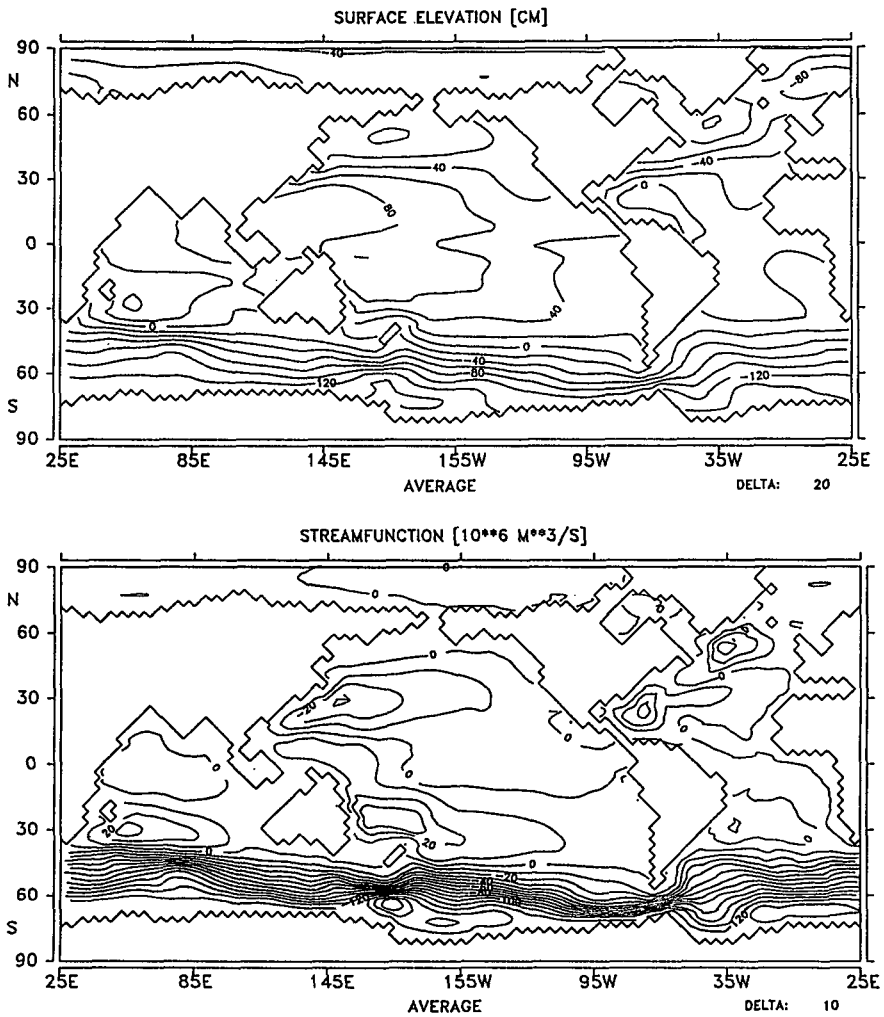

FIG. 4. (a: top) Surface topography and (b: bottom) mass transport streamfunction.

density. The higher salinity of the Atlantic relative to the Pacific leads to a 80-cm higher sea level in the Pacific than in the Atlantic. Figure 4b shows the vertically integrated annual-mean mass transport streamfunction. The most pronounced feature is the strong Antarctic Circumpolar Current, which is associated with a large change of the surface elevation. The structure of the subtropical gyres is reproduced reasonably well.

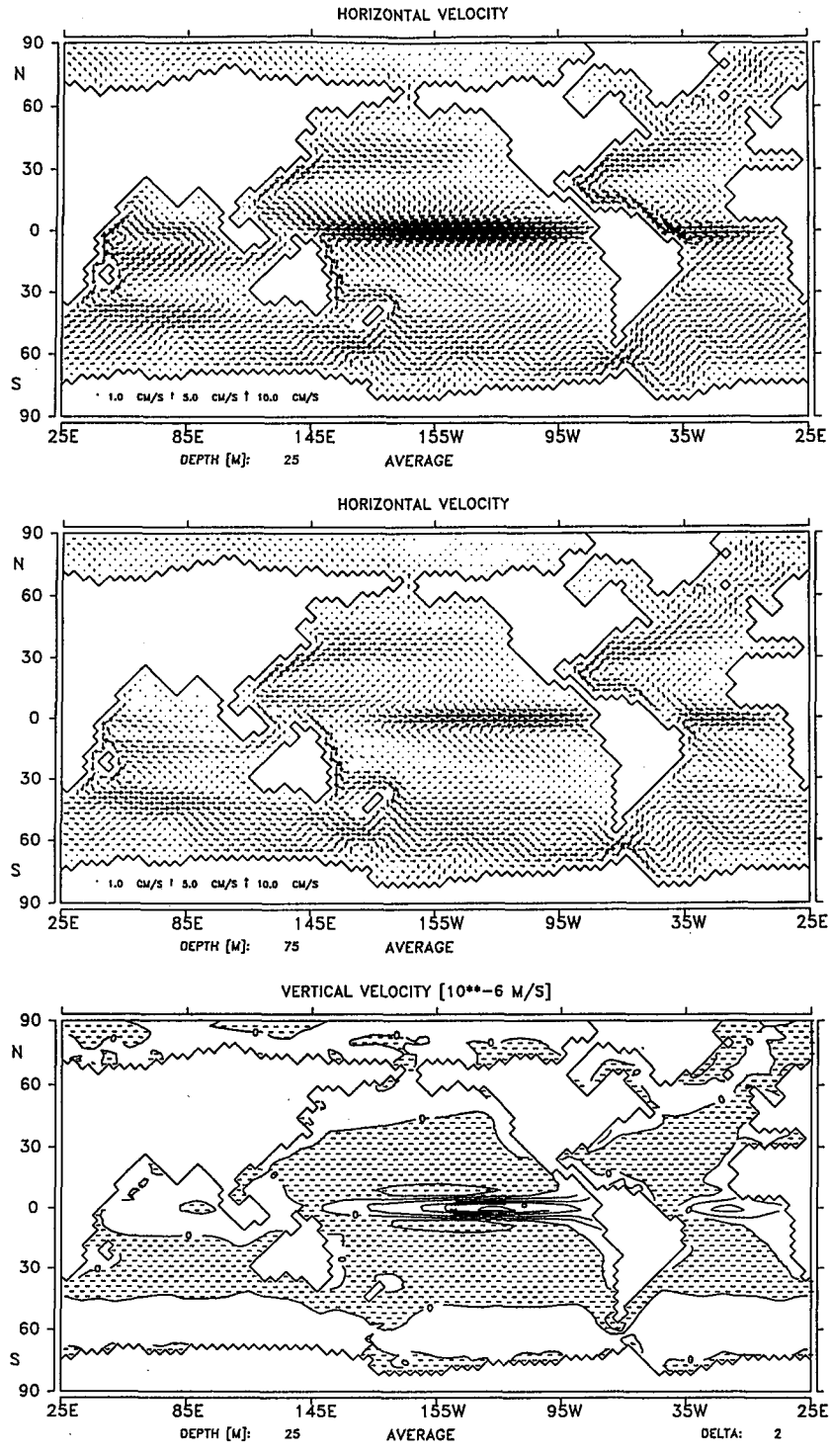

FIG. 5. Horizontal velocity in (a: top) the surface layer, horizontal velocity in (b: middle) the second layer, and (c: bottom) vertical velocity below the first layer.

The Gulf Stream, however, is underestimated by a factor of 2 (which is typical for coarse resolution non-eddy-resolving models).

The basic structure of the annual mean near-surface circulation is shown in Fig. 5. In the surface layer, the horizontal velocities (Fig. 5a) consist of a superposition of the Ekman drift and the geostrophic current. The principal ocean surface current systems are reproduced except around the equator where details of the countercurrent systems could not be resolved. The currents in the second layer (Fig. 5b) closely follow the surface currents, except along the equator, where, despite the limited resolution and missing nonlinear advection of momentum, a pronounced eastward undercurrent is simulated (although broader and more sluggish than in nature). The vertical velocity at the 50-m level is shown in Fig. 5c. It is determined by the divergence of the net surface current, which at this level is dominated by the Ekman transport.

The structure of the water mass transport in deeper levels is best represented by the flow field along surfaces of constant density. As potential density should be conserved in a nonmixing deep ocean below the mixed layer, all water parcel trajectories should follow these surfaces rather closely. Figures 6a,b show the depths of the isopycnal surfaces σ_ϑ = 26.5 and σ_2 = 36.96,

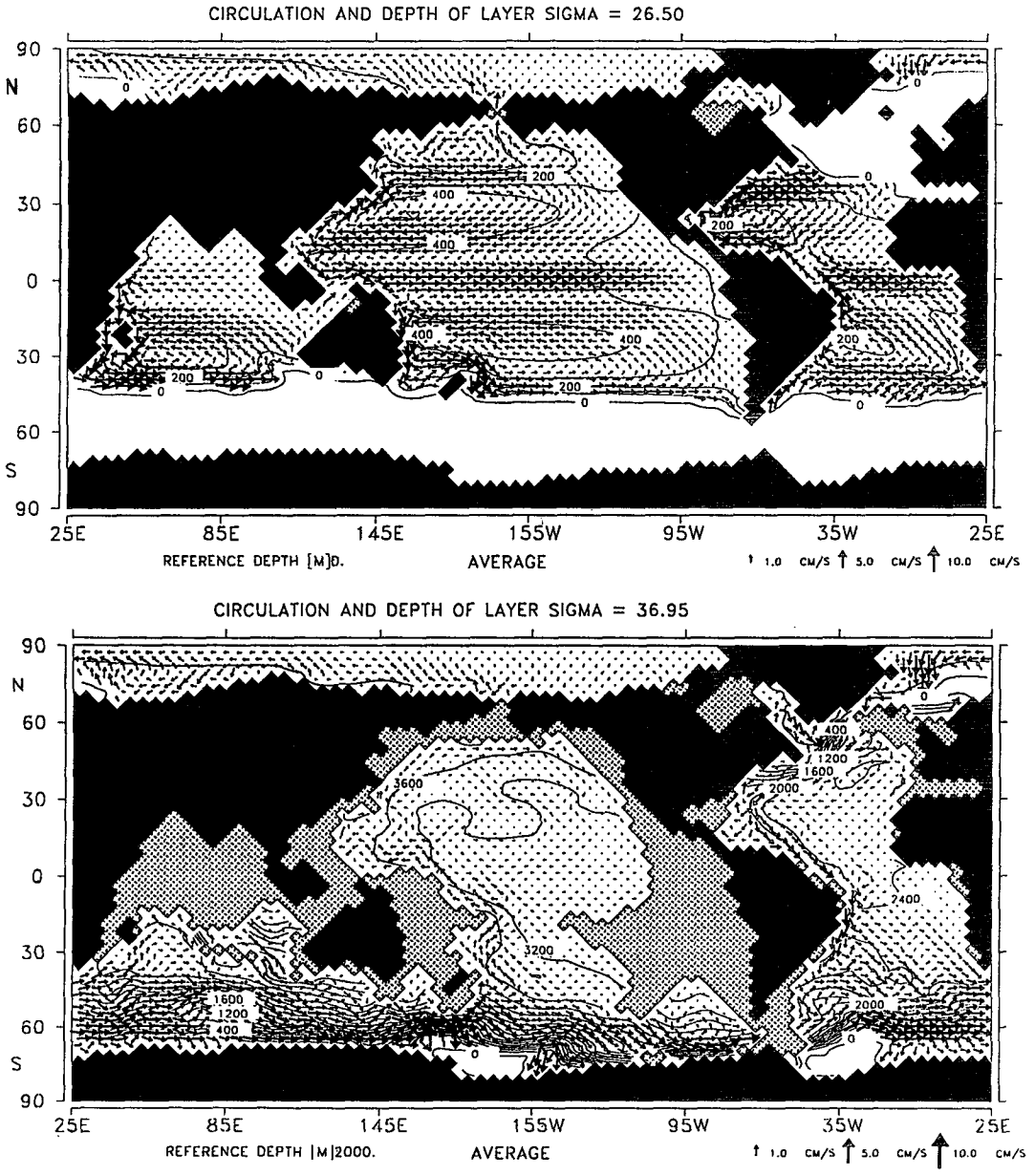

FIG. 6. Depth of the layer (a: top) σ_ϑ = 26.5 and (b: bottom) σ_2 = 36.95 and circulation in respective horizon.

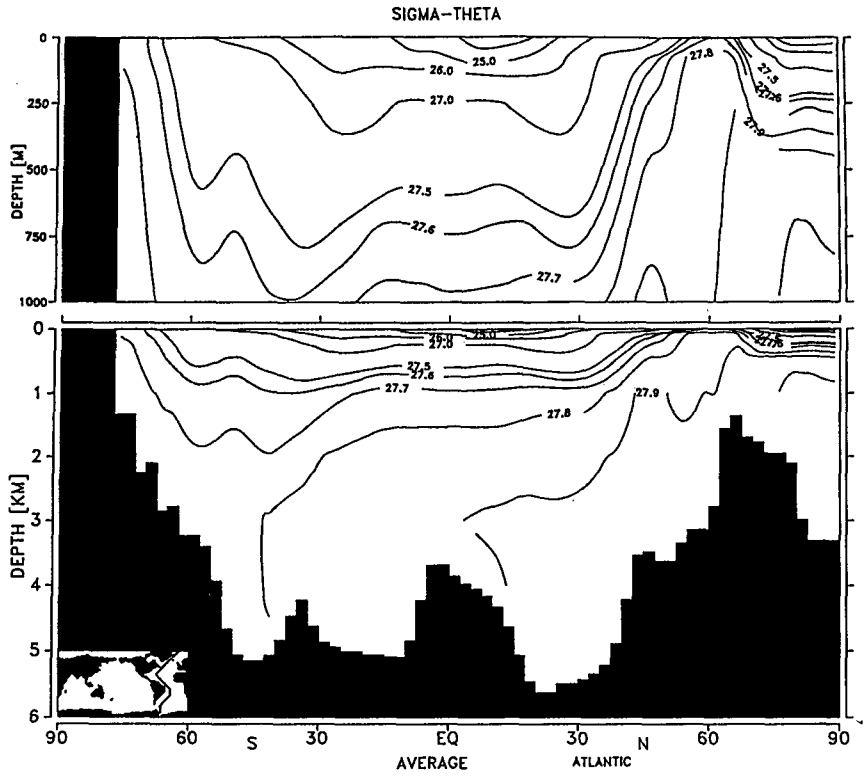

FIG. 7a. σ_ϑ in a section of the western Atlantic.

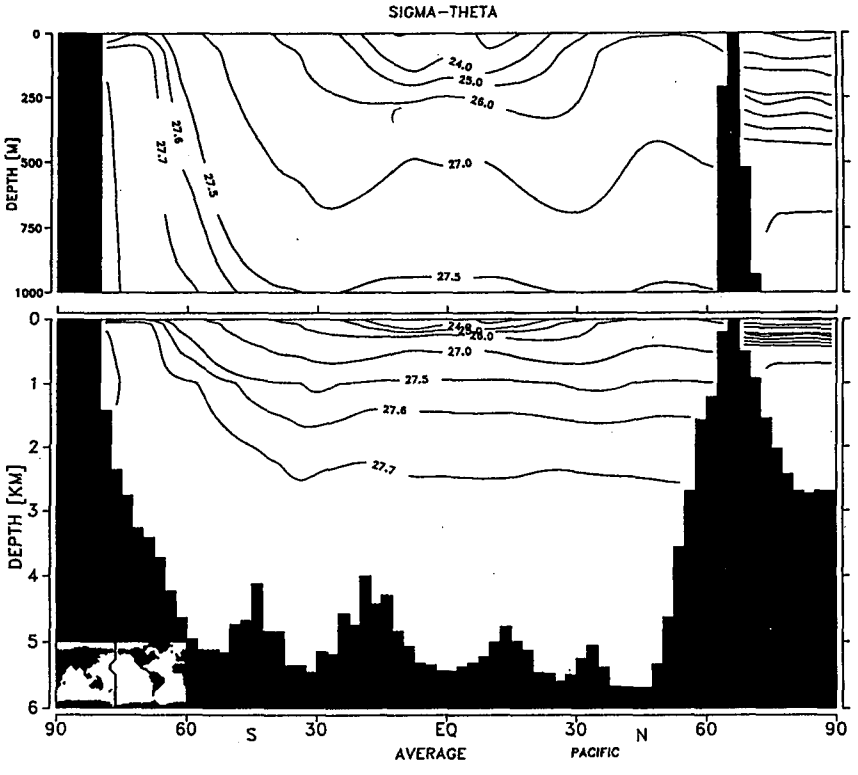

FIG. 7b. σ_ϑ in a section of the western Pacific.

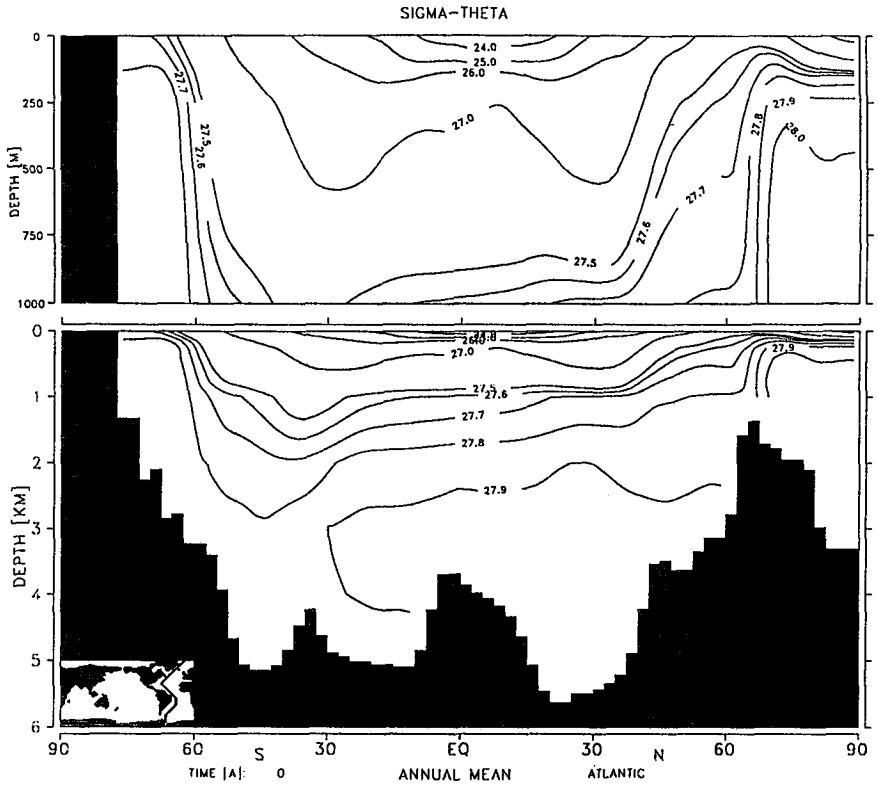

FIG. 7c. Same as Fig. 7a from the Levitus dataset.

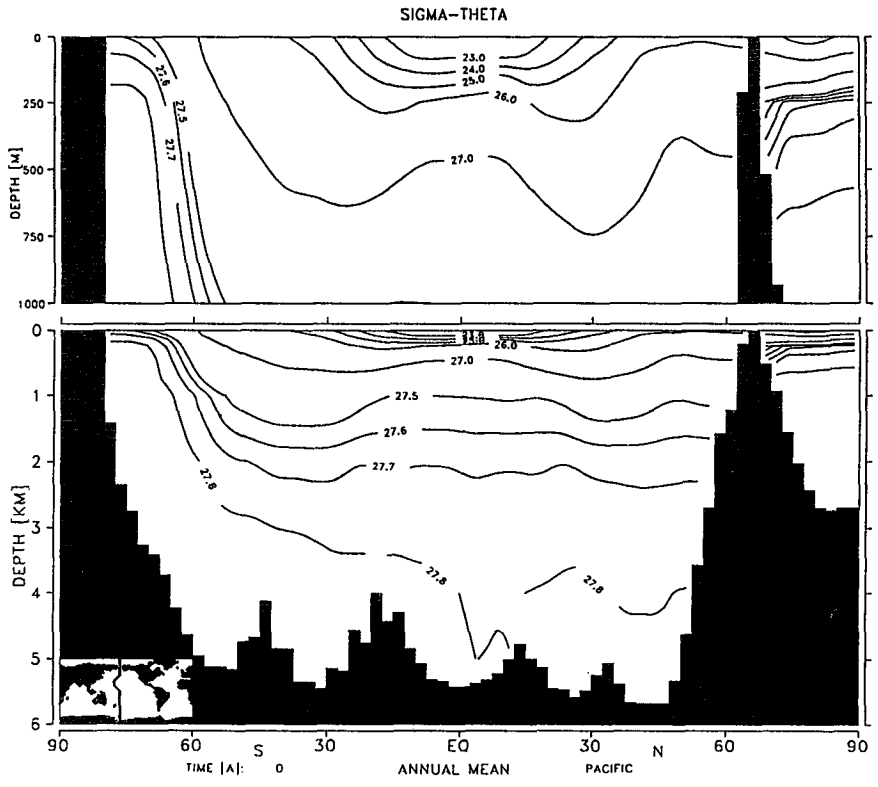

FIG. 7d. Same as Fig. 7b from the Levitus dataset.

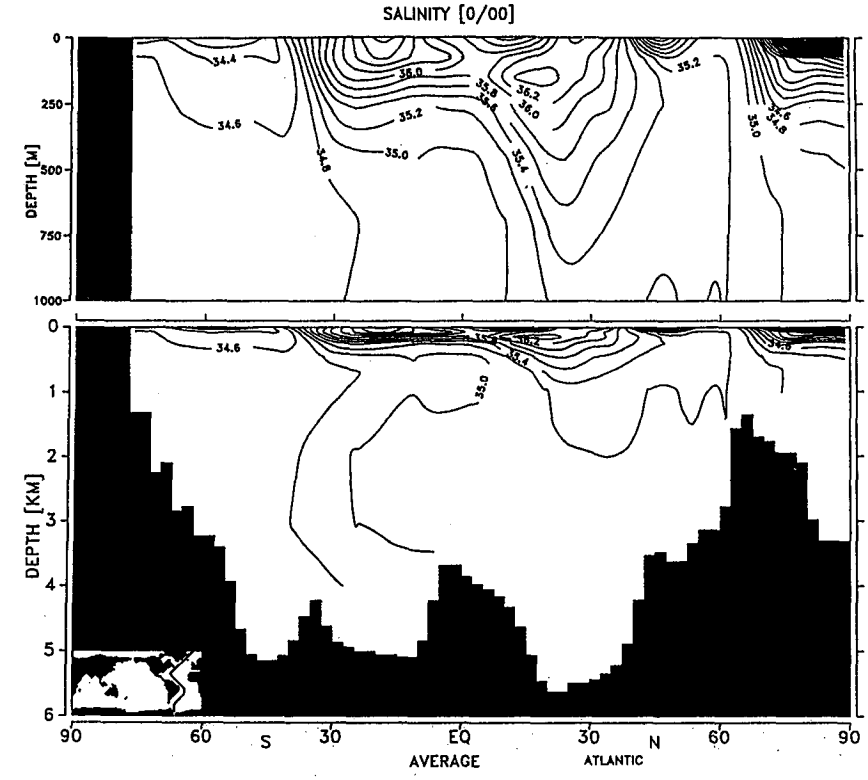

FIG. 7e. Salinity section in the western Atlantic.

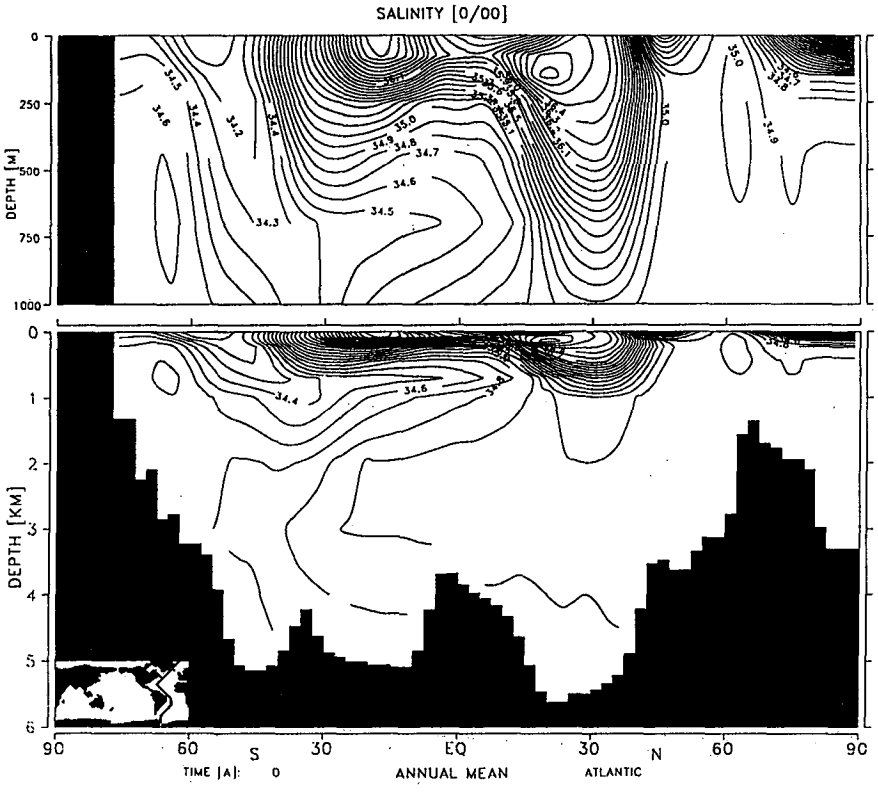

FIG. 7f. Same as Fig. 7e from the Levitus dataset.

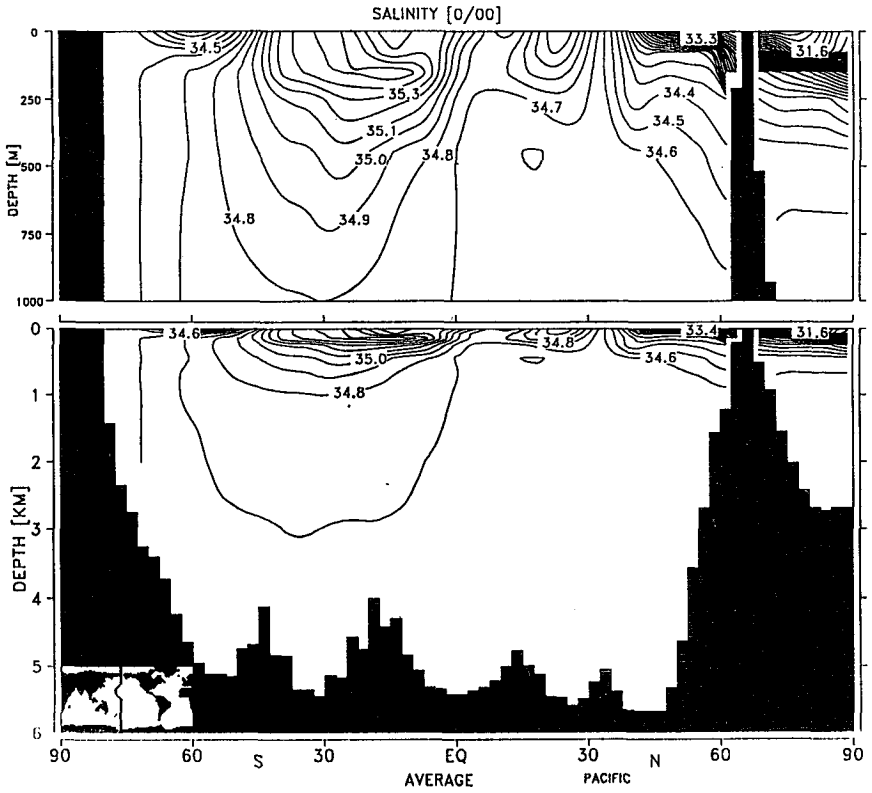

FIG. 7g. Salinity section in the western Pacific.

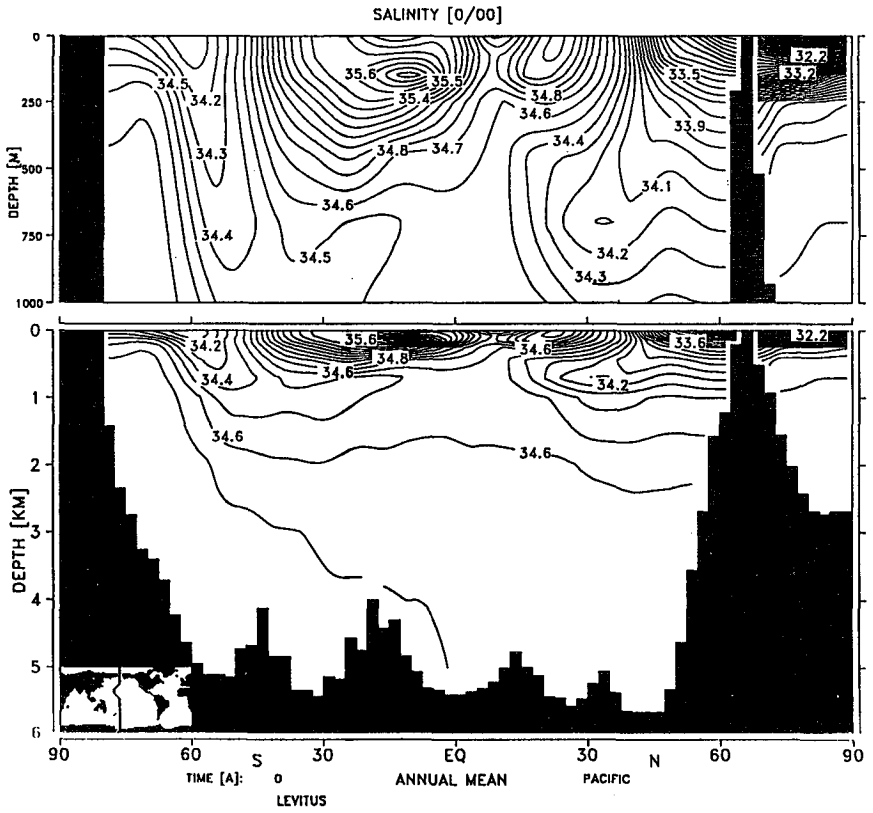

FIG. 7h. Same as Fig. 7g from the Levitus dataset.

respectively, together with the associated horizontal velocity fields. The surface $\sigma_\vartheta = 26.5$ characterizes the main thermocline gyres and the equatorial undercurrent, while the isopycnal $\sigma_2 = 36.95$ lies in the deeper ocean. For this level, the 2-km reference-depth potential density σ_2 was chosen rather than the surface reference level, since σ_ϑ is no longer appropriate because of the nonlinearity of the equation of state [cf., for example, the GEOSECS (Bainbridge 1981) section for σ_ϑ in the Atlantic, which displays a spurious apparent instability in the deep southern region through this effect]. The equatorial upwelling region and the depression of the isopycnals in the main gyres are clearly seen. In most regions of the ocean, the flow follows the constant depth contours, but isobaths are crossed in areas of upwelling and downwelling. Near the outcropping boundaries, however, variations in the isopycnal depth are generally the result of water mixing rather than adiabatic rising or sinking motions.

Figures 7a,b show two sections of σ_ϑ in the Pacific and Atlantic computed from S and T. The most outstanding feature is the doming of the isopycnals across the equator (the apparently unstable stratification in the deep Atlantic is again spurious and arises from the difference in the gradients of σ_4 and σ_ϑ). The observed data show, additionally, a pronounced tongue of Antarctic Intermediate Water, especially in the South Atlantic salinity. This structure appears also in the model, but is underestimated.

These sections can be compared with the corresponding sections of the Levitus dataset displayed in Figs. 7c,d. The model results agree well with the climatological dataset, although the depth of the main pycnocline is underestimated. The agreement is poorer, however, if the temperature and salinity are regarded separately. The temperature and salinity errors seem to partially compensate for each other in the density fields. Figures 7e,f show the Atlantic sections of salinity from the Levitus data and from the model. The general structure is well reproduced; the model's salinity, however, is slightly too high, as seen most clearly in the tongue of Antarctic Intermediate Water. Figures 7g,h show the corresponding sections for the Pacific. The distributions are horizontally more uniform than in the Atlantic. In the Southern Ocean the data contain an intermediate area of low salinity, which is not reproduced by the model. The origin of this water mass is less obvious than in the Atlantic (cf. Reid 1986), and its impact on the tracer distributions is smaller. In the Atlantic, the AAIW is seen in all tracers, whereas the intermediate water of the southern Pacific is evident only in the distributions of salt and alkalinity but not in the distributions of phosphate and oxygen (Bainbridge 1981; Craig et al. 1981).

The surface fluxes of fresh water and heat, computed diagnostically from the boundary values of salinity and temperature, are shown in Figs. 8 and 9. Characteristic regional features, such as the evaporation in subtropical gyres and increased precipitation in the North Pacific, are reproduced as expected. In the polar regions, the freshwater flux is influenced by changes in the ice budget, in addition to the evaporation-minus-precipitation budget.

The seasonal heat flux distributions (Fig. 9, for January and July) exhibit strong regional variations (for example, in the South Pacific), which are not easily interpreted. However, these variations largely cancel out in the annual-mean heat flux (Fig. 10), which resembles rather closely the pattern derived from observations (e.g., Esbensen and Kushnir 1981 or Oberhuber 1988). The seasonal cycle of the zonally integrated heat flux (Fig. 11) also agrees, in essence, with observed data.

Figure 12 shows the zonally integrated meridional transports of heat and fresh water in the three separate ocean basins. The absolute values of the heat transport

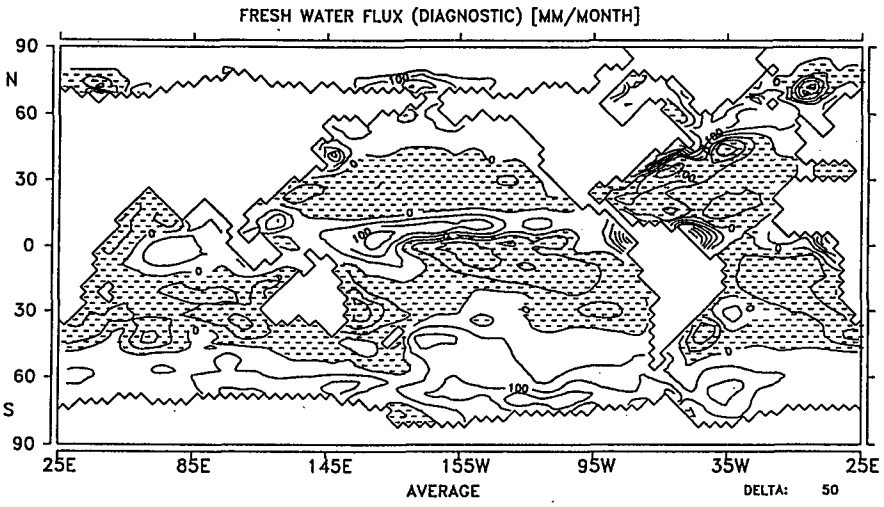

FIG. 8. Freshwater flux as determined diagnostically from the salinity boundary condition.

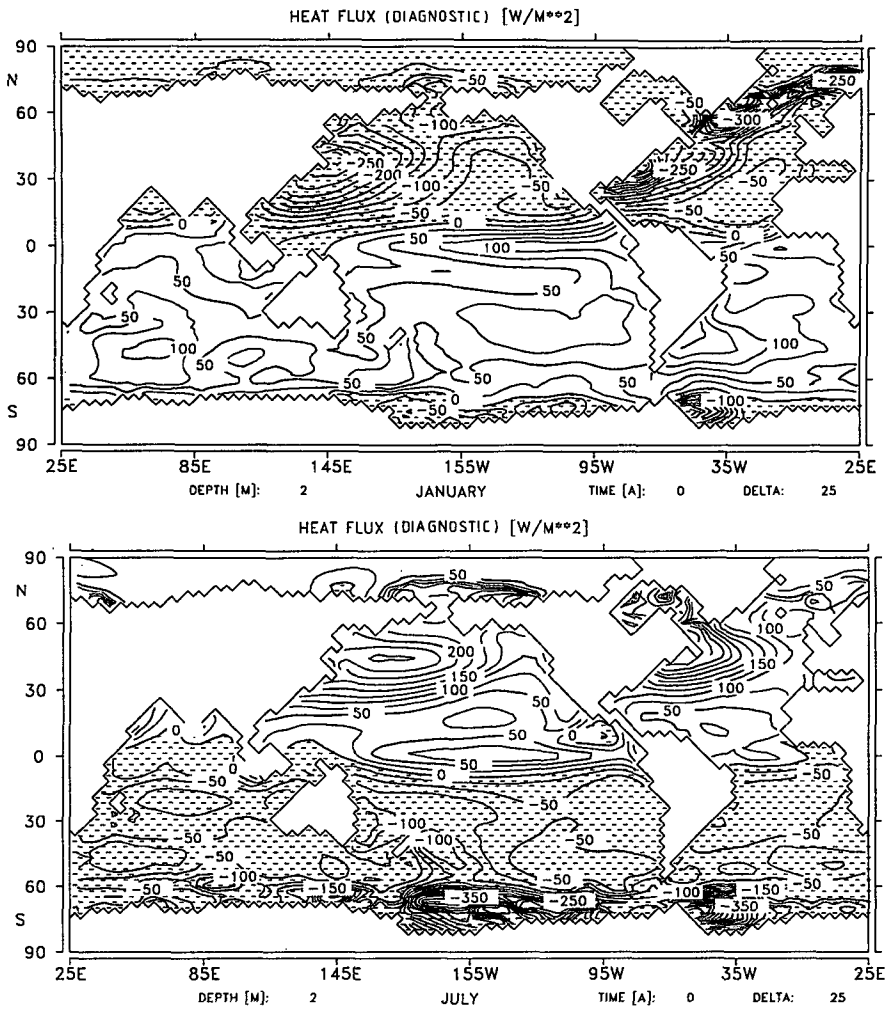

FIG. 9a. Heat flux as determined diagnostically from the temperature boundary condition for (a: top) January and (b: bottom) July.

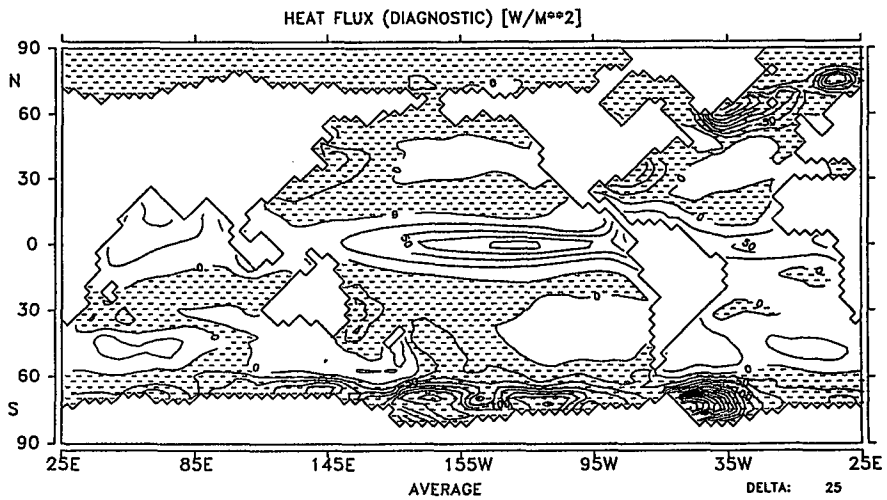

FIG. 10. Same as Fig. 9 but for annual mean.

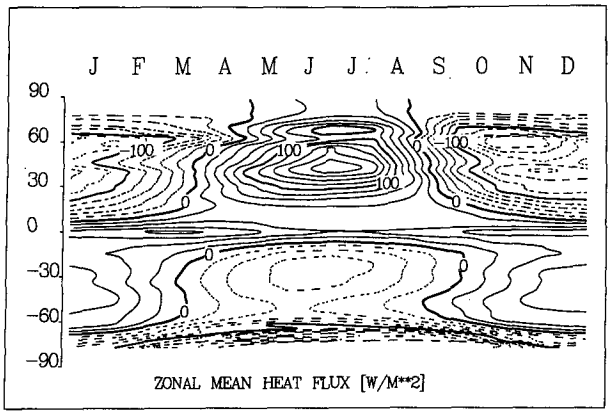

FIG. 11. Seasonal cycle of the zonally integrated heat flux.

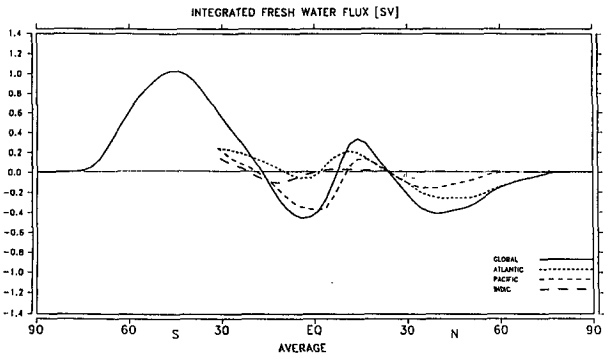

FIG. 12b. Integrated freshwater flux out of the ocean.

are at the lower bounds of observations (cf. Roemmich and Wunsch 1985). This is consistent with the relative shallowness of the model thermocline. The striking differences between the circulation patterns in the different ocean basins, discussed already in terms of the "conveyor belt" picture, appear also in the meridional transports. The Atlantic exhibits a substantial northward heat transport in both hemispheres, extending across the equator up to Iceland, whereas the heat transport of the northern Pacific is very small outside the equatorial Ekman circulation region.

4. Sensitivity with respect to temperature and salinity surface boundary conditions

Now we investigate the dependence of the ocean circulation on alternative formulations of the boundary conditions for heat and salt. In addition to the standard run ATOS1 (Atmospheric Temperature, Ocean Salt and atmospheric temperature advection with reference factor 1), four additional experiments were carried out (cf. Table 1). These differed in the temperature boundary condition {coupling to the observed ocean surface temperature in OTOSE, OTOSD or to the observed atmospheric surface temperature with different restoring factors [λ in Eq. (15) in ATOS0/1/2]} and in the relaxation time constants used for the temperature and salinity boundary conditions. All cases could be regarded as acceptable interpretations of climatology and could, therefore, be expected intuitively to give similar results. However, the simulations were, in fact, found to differ significantly. The most pronounced differences between the five experiments appeared in the circulation regime of the deep ocean. This strongly affects the residence times of tracers, the rate of uptake of CO_2 by the oceans, the heat and freshwater transports (which are intimately linked with the meridional overturning). The deep-ocean temperatures and salinities also differ to some extent (Fig. 13). However, it is difficult to judge the model performance from these fields alone, as the observed deep-ocean values could well represent the response to ocean surface conditions several hundred years ago (during the Little Ice Age).

The ocean currents and density stratification in the upper ocean are only weakly influenced by the modifications in the boundary conditions. It appears that the main wind-driven gyres are not very sensitive to the form of the heat and freshwater flux boundary condition (the wind stress was not changed in the sensitivity experiments shown, but in other simulations with modified wind fields significant changes in the ocean gyres were not found).

Figure 14 shows a comparison of the meridional overturning streamfunctions of the Atlantic circulation at 30°S for the five experiments. While the standard run ATOS1 produces a deep southward flow of 22 Sv below a depth of 1.5 km in the North Atlantic—which is the source of the classical "conveyor belt" transport into the South Atlantic, the Indian Ocean, and the Antarctic Circumpolar Current—the experiments OTOSE, OTOSD, and ATOSO all fail to provide an adequate source of North Atlantic deep water. The cold deep water in the Atlantic flows northward in these experiments from a source in the Southern Ocean. The experiment ATOS2 is similar to ATOS1 but exhibits, as expected, a too strong, southward, deep Atlantic flow.

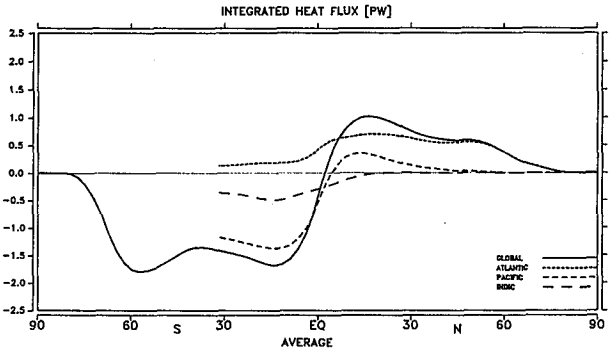

FIG. 12a. Zonally integrated transport of heat (annual mean).

TABLE 1.

Name	OTOSD	OTOSE	ATOS0	ATOS1	ATOS2
Restoring time constant (d)					
Salinity	1500	30	40	40	40
Temperature	30	30	60	60	60
Forcing temperature	SST	SST	air	air	air
Sea ice model	no	no	yes	yes	yes
Air temperature restoring time constant (s) λ^{-1}	—	—	0	1.2×10^5	2.4×10^5

In comparison with observed data, the differences in the flow regimes are best seen in the geochemical tracers. Figure 15 compares the computed ^{14}C distribution for ATOS1 with the measurements of Östlund and Stuiver (1980) and Stuiver and Östlund (1980). An accurate computation of ^{14}C distributions requires a three-dimensional carbon cycle model (cf. Maier-Reimer and Hasselmann 1987; Bacastow and Maier-Reimer 1990). For the present comparative purposes, however, a simplified ^{14}C tracer model without a biological pump appeared adequate. The ^{14}C was assumed to enter the ocean from the atmosphere at an initial concentration of 1000 units with a constant piston velocity of 7.5 m yr^{-1}. This corresponds closely to the treatment of ^{14}C by the Princeton Group (Toggweiler et al. 1989). It was then advected by the (previously computed) mean ocean circulation, while decaying with an e-folding time of 8267 years. The vertical mixing by convection was estimated from the (also previously computed) frequency and intensity of convective mixing in the ocean circulation run. Since in this simplified simulation the input of radiocarbon from the nuclear weapon tests in the early 1960s is disregarded, the upper half-kilometer and the Northern Atlantic north of 40°N are excluded from the comparison of model results with data. The conveyor belt structure of the global deep circulation is clearly manifested in the age difference between Atlantic and Pacific. The gradients in the individual oceans between 40°S and 40°N are realistically simulated by the model. In the ACC, however, the model radiocarbon is too young. This discrepancy indicates that the overall convection in the Southern Ocean is overestimated by the model.

In Fig. 16 we compare the results of the five experiments with the GEOSECS data along the section in the western Atlantic in 3-km depth, which is approximately the core of the real NADW. For the assessment of the circulation fields, the gradients are more important than the absolute values, which depend strongly on our rather simple assumption on the iso-

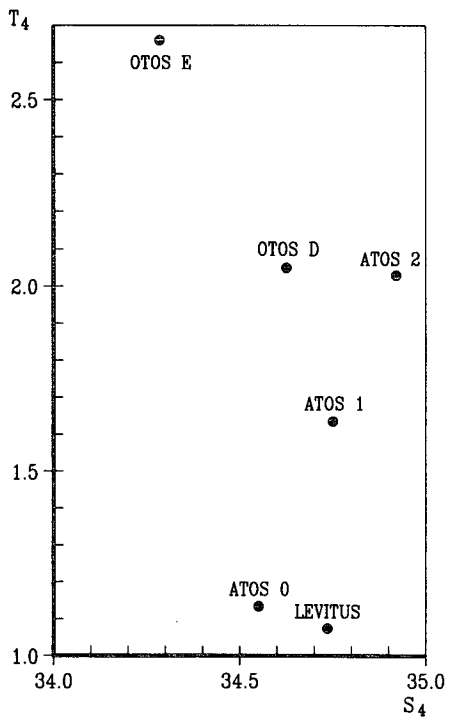

FIG. 13. Global averages of temperature and salinity at a depth of 4 km for the five experiments and from Levitus.

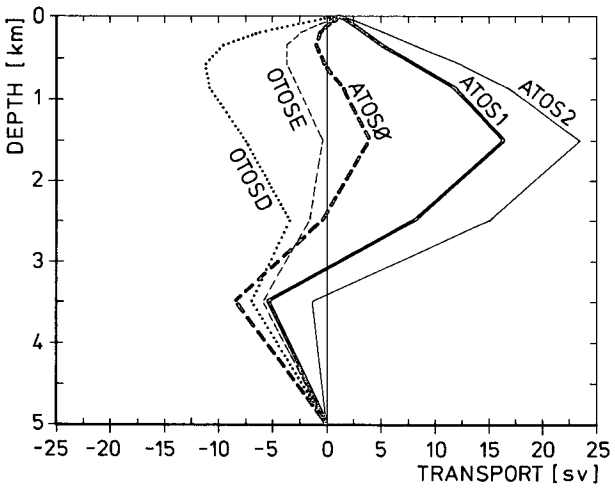

FIG. 14. Zonally integrated flow across 30°S in the Atlantic for the five experiments. Here "\" denotes northward flow; "/" means southward. The offset at $z = 0$ is in balance with inflow from the Bering Strait and with net evaporation.

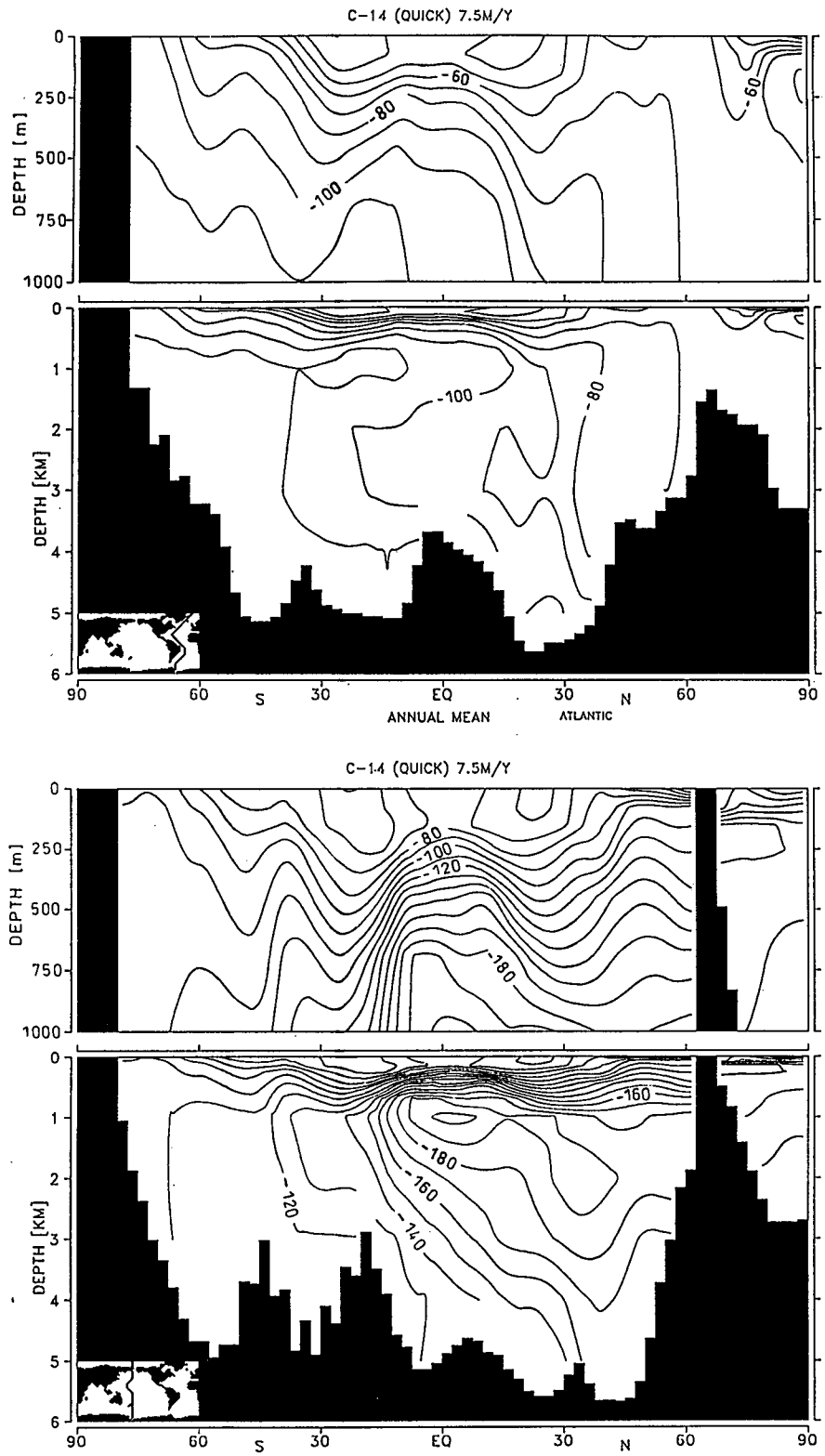

FIG. 15. Radiocarbon in (a: top) the western Atlantic and (b: bottom) the western Pacific for the standard run.

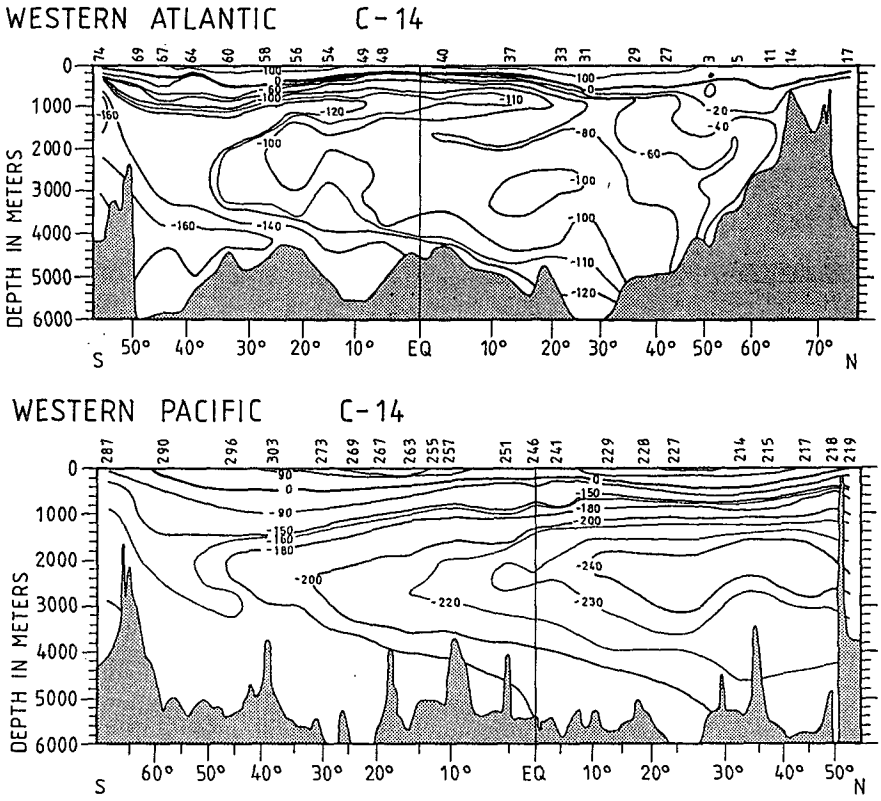

FIG. 15. (*Continued*) Same as (a) and (b) panels but from GEOSECS (after Stuiver and Östlund 1980).

topic gas transfer velocity. The closest agreement with the observations is found in the standard run ATOS1 (Fig. 16). Experiments OTOSE, OTODS, and ATOS0, which have insufficient North Atlantic deep-water formation, fail to reproduce the characteristic tongue of young deep water extending southward into the South Atlantic. The differences in the Pacific are less pronounced, but here also the standard run yields the best agreement.

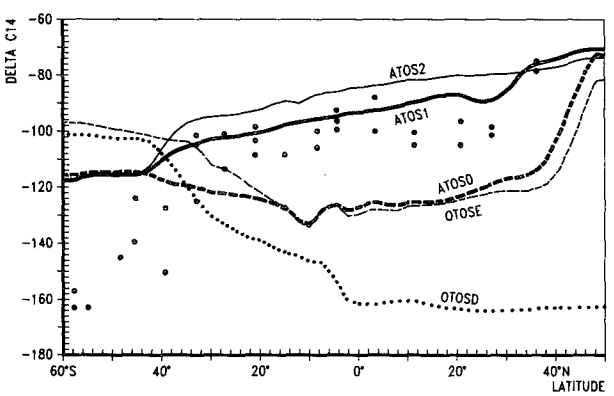

FIG. 16. Radiocarbon along a section in the western Atlantic for the five experiments and the GESOSECS data in 3-km depth.

Figure 17 summarizes the principal differences between the five experiments in terms of six selected circulation indices. The experiments are ordered with respect to the first index, plotted on the abscissa axis, representing the fraction of the total potential energy release by convective mixing that is provided by the Southern Oceans. The remaining five indices, plotted (with five different scales) on the ordinate axis, represent:

(i) The North Atlantic convective energy release (NACE);
(ii) the Southern Ocean convective energy release (SOCE);
(iii) the North Atlantic meridional heat transport at 30°N, the latitude of maximal heat flux (NAHT);
(iv) the (southward) Southern Ocean heat transport at 30°S (SOHT); and
(v) the North Atlantic outflow of deep water across 30°S (NAOF).

The curves demonstrate the major changes in all six indices brought about by the relatively minor differences in the surface heat flux forcing.

All circulation indices are seen to vary monotonically with the north–south partitioning of the total convective energy release. Following the sequence of the five

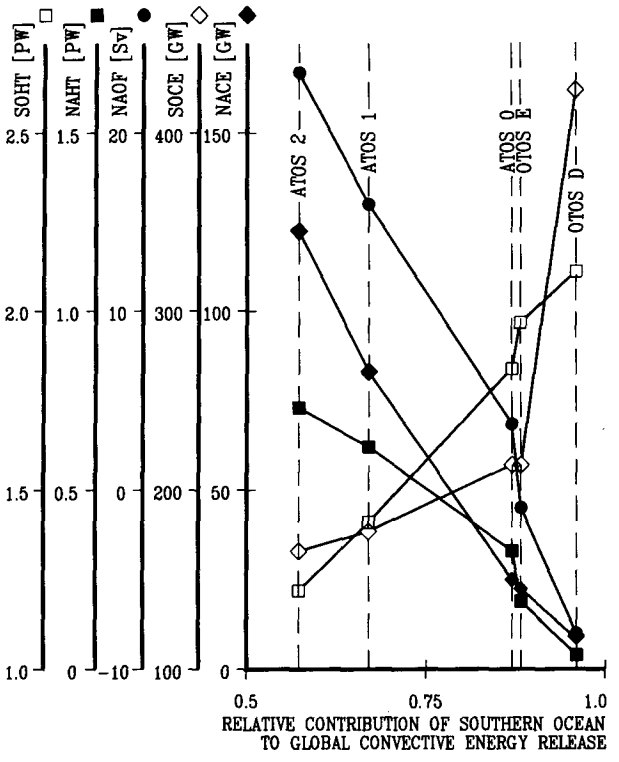

FIG. 17. Circulation indices as a function of fraction of the total potential energy release by convective mixing provided by the Southern Ocean.

experiments ATOS2 to OTOSD from left to right, the convective energy release in the North Atlantic decreases continuously, while the convective energy release in the Southern Ocean increases. The deep outflow from the North Atlantic and the Atlantic heat flux both decrease through the sequence, while the total heat flux at 30°S increases. Note that the sum of SOHT and NAHT is almost constant in our experiment due to the similar action of the different boundary conditions in the tropics, where the ocean is heated at the surface. The effective freshwater fluxes were almost identical in the experiments with the strong restoring to the surface salinity from the Levitus data; in the experiment OTOSD with the restoring constant 50 times weaker, the amplitude of the freshwater flux is reduced by a factor on the order of 5.

In essence, the sequence of experiments describes a gradual transition from a deep-ocean circulation regime characterized by a strong southward "conveyor belt type" transport in the Atlantic to a circulation regime in which the deep Atlantic is relatively stagnant and most of the deep-water formation occurs in the Antarctic. The changes are brought about by changes in the rate of deep-water formation in high latitudes, which are extremely sensitive to small changes in the air–sea heat exchange. Although the most obvious signatures are seen in the abyssal circulation, significant changes also occur in the climatically important heat fluxes through the air–sea interface, as evidenced by the large, relative changes in the meridional heat fluxes in the North Atlantic and, to a smaller extent, in the Southern Ocean.

The changes affect also the uptake of CO_2 by the ocean. The impulse response function describing the response of the atmospheric CO_2 concentration to a δ-function injection of CO_2 into the atmosphere, for example, is characterized by a 50% larger time constant ($\sim$150 years) for a coupled atmosphere–ocean carbon cycle model based on the standard circulation ATOS1 than the time constant found by Maier-Reimer and Hasselmann (1987) in their original model, which was based on the circulation OTOSD with a stronger Antarctic overturning.

The sensitivity of the ocean uptake of CO_2 to changes in the ocean circulation, and the sensitivity of the ocean circulation in turn to changes in the atmospheric forcing, imply that computations of climatic change produced by anthropogenic CO_2 emissions should be carried out, if possible, with a fully coupled three-dimensional global ocean–atmosphere–carbon cycle model.

5. Conclusions

The principal conclusions of our study may be summarized as follows:

1) An economical global ocean circulation model with 3.5° × 3.5° horizontal resolution, 11 vertical layers, and a time step of 1 month based on large-scale geostrophic dynamics is able to reproduce most of the principal observed water mass properties of the global ocean circulation, including salinity, temperature, and tracer (e.g., $\Delta^{14}C$) distributions, and water mass and heat transports;

2) The circulation is very sensitive to small changes in the high-latitude heat flux. These can produce large changes in the relative rates of deep-water formation in the North Atlantic and Southern Ocean, leading to a transition from the present circulation regime, characterized by a dominant deep-water source in the North Atlantic, to a circulation regime, which may have been more typical of previous climate epochs, in which the Antarctic Circumpolar Front represents the major deep-water source.

3) The sensitivity with respect to the parameterization of the heat flux is consistent with previous findings of the sensitivity of the ocean circulation to changes in the freshwater flux (Maier-Reimer and Mikolajewicz 1989; Mikolajewicz and Maier-Reimer 1990).

4) The simulations provide support for the view that at least two equilibrium states of the ocean circulation exist, which are characterized by different rates of deep-water formation in the two hemispheres, and that the transition from one circulation regime to another can be brought about by relatively low thresholds of external forcing.

Acknowledgments. We thank Dirk Olbers and Jürgen Willebrand for tireless support and continuous advice over a long period during which the model was developed. We are grateful to Wallace Broecker for enthusiastic encouragement and enlightening criticism during a visit to the Max-Planck Institute in a critical phase of the model testing. We also thank Marion Grunert and Heinke Hoeck for their assistance in preparing the figures. The work was supported, in part, by grants from the climatic programs of the Bundesminister für Forschung und Technologie (Grant No. 07kft470) and the Commission of the European Community (Grant No. EV4C0035-D).

APPENDIX A

Decomposition into Modes

For simplicity the deviations from a uniformly rotating plane are neglected in this section. The linearized equations of inviscid motion on an f plane are

$$(\partial_t u_{ik} + f\epsilon_{ij}u_{jk}) + \partial_i p_k = 0, \qquad \text{(A1)}$$

where u_{ik} are the horizontal components of velocity at level k; f is the Coriolis parameter; p_k is the pressure normalized by ρ_{0k}, the reference density of layer k according to the Boussinesq approximation; and ϵ_{ij} is the antisymmetric tensor. The number of layers is N.

The hydrostatic approximation yields the pressure

$$p(z) = g\rho_{00}\zeta + \int_z^0 g\rho(s)ds. \qquad \text{(A2)}$$

A density anomaly $\delta\rho$ at depth D contributes $g\delta\rho(B - D)/B$ to the forcing of the barotropic motion, $+g\delta\rho D/B$ to all baroclinic motion below D, and $-g\delta\rho(B - D)/B$ to the baroclinic motion above D.

For the formulation of the implicit time discretization we perform the transformation

$$V_1 = \sum_{k=1}^{N} \Delta z_k u_k,$$

and

$$V_k = H_k(u_k - u_{k-1}), \quad k = 2, \cdots, N,$$

where $H_k = D_k(B - D_k)/B$, and $D_k = \sum_{n=1}^{k-1} \Delta z_n$ ($D_1 = 0$) corresponds to the reduced depth of a two-layer mode defined at the depth D_k.

The inverse transformation is given by

$$u_k = \sum_{n=1}^{k} V_n/(B - D_n) - \sum_{n=k+1}^{N} V_n/D_n.$$

The layer thickness Δz_k is normally defined by the computation levels; however, at locations where the assumed topography intersects the levels of computation, a modified layer thickness is introduced in order to obtain smoother variations of depth than could otherwise be achieved for the low number of levels of our model. Figure A1 shows the models resolution in the northern Atlantic at 30°N.

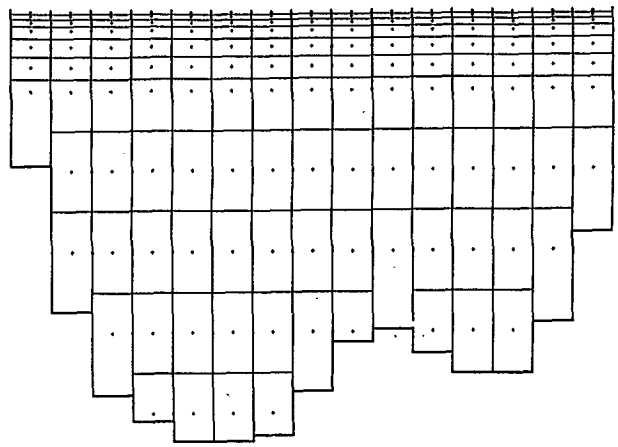

FIG. A1. Position of grid points on 30°N in the Atlantic.

Here V_1 is the barotropic mode, while for $k > 1$, V_k represent the $N - 1$ computational baroclinic modes of the model grid. They are driven by the vertical shear of the horizontal pressure gradients, that is, the local density gradients. Each of the baroclinic modes represents a flow field with vanishing $\int udz$.

For the time discretization, the modes are treated separately. For each mode $k \geq 2$, the convergence $W_k = \partial_i V_{ik}$ creates a profile of vertical velocity at levels m:

$$w = 0 \quad \text{at the bottom}$$

$$w_{km} = \begin{cases} W_k(D - D_m)/(D - D_{k-1}), & \text{for } D_m > D_{k-1} \\ W_k D_m/D_{k-1}, & \text{for } D_m < D_{k-1}. \end{cases} \qquad \text{(A3)}$$

(For $k = 1$, w at the surface is the rate of change of sea level.) The vertical velocity profiles w_{kl} with $k \neq l$ provide the coupling between the different modes with a one time step delay.

The decoupled mode equations can be written:

$$\partial_t V_i + f\epsilon_{ij}V_j + \partial_i p = F \qquad \text{(A4)}$$

$$\partial_t p + c^2\partial_i V_i = 0, \qquad \text{(A5)}$$

where the phase velocity c is determined by the overall stratification, but with the strongest contribution coming from the level associated with the mode under consideration (including the air–sea difference of density for the barotropic mode).

For the experiments described in this paper, the Euler backward procedure was rigorously applied, in which the time discretization $\partial_t(V, p) = \tau^{-1}((V, p)^t - (V, p)^{t-\tau})$ links the variables at t. Insertion of (A5) and (A3) into (A4) yields

$$\partial_t V_{ik} + H_k f\epsilon_{ij}V_{jk} + (g/\rho_{0k})\partial_i F'_k = 0,$$

with $F' = D'_k\rho_k + \tau \sum D'_l w_{kl}(\rho_k - \rho_{k-1})$. Replacing

all abbreviations by their definitions, we obtain finally an elliptic system of the form:

$$\tau^{-1}V_1 - fV_2 - \tau c^2(\partial_{11}V_1 + \partial_{12}V_2) = F_1$$
$$\tau^{-1}V_2 + fV_1 - \tau c^2(\partial_{22}V_2 + \partial_{12}V_1) = F_2, \quad \text{(A6)}$$

where F contains the density field at the beginning of the time step, frictional forces, and the wind stress for the barotropic and the first baroclinic mode.

For the baroclinic modes the system is solved by iteration. Because of the error damping associated with the discretization, there is no need for very high accuracy; the iteration is stopped after 12 sweeps, which reduce the error of the first guess (the values of the preceding time step) to approximately 5%.

For the barotropic mode the convergence is very slow, so that the equations are solved directly by elimination. The matrix is triangularized once for the initial stratification. As the matrix is sparse, there is no need for pivoting. The matrix retains the band structure in the triangularization. The triangularized band matrix enables a rather efficient solution of (A6) at each time step of the integration.

APPENDIX B

Wave Dispersion

For each mode the implicit discretization can be written formally as the simplified system:

$$u^t - f\tau v^t + \partial_x p^t \tau = u^{t-\tau}$$
$$v^t + f\tau u^t + \partial_y p^t \tau = v^{t-\tau}$$
$$p^t + c^2\tau(\partial_x u^t + \partial_y v^t) = p^{t-\tau}.$$

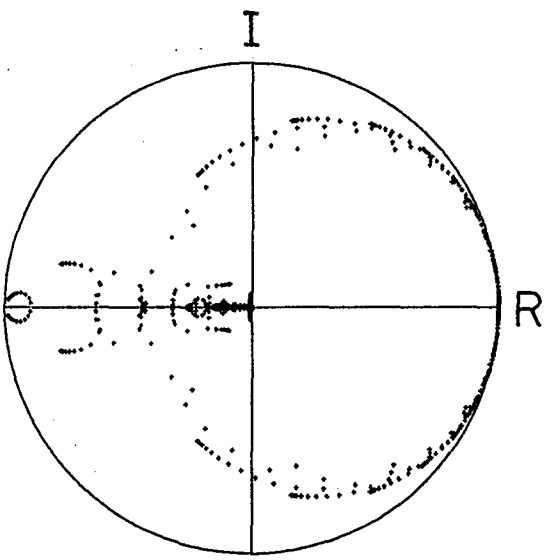

FIG. B1. Location of the eigenvalues in the complex plain of the Euler backward scheme for gravity wave phase speed c = 1 m/s Δx = 500 km and Δt = 30d.

Outside the equatorial belt, $f\tau \gg 1$ and we can neglect the momentum acceleration. Then

$$p^t = p^{t-\tau} - \tau c^2(u_x + v_y),$$
$$\text{with} \quad v = p_x^t/f \quad \text{and} \quad u = -p_y^t/f.$$

For any wavelike disturbance $p^{t-\tau} = P_0 \exp[i(kx + my)]$ we have

$$p^t = P_0 \exp[i(kx + my)]/(1 + \beta ik\tau c^2/f^2),$$

which for small c is a good approximation for the exact expression $p^{t-\tau} \exp(-i\beta kc^2\tau/f^2)$, valid for waves whose wavelength is large compared with the Rossby radius of deformation.

Near the equator this approximation is not valid. The eigenvalue analysis was performed for a wavelike disturbance $\exp(ikx)$ for all variables in an equatorial channel with 12 grid points on each side of the equator. Figure B1 shows the location of the eigenvalues in the complex plane for the space and time steps of our model and for a typical phase speed of 1 m s^{-1} for the gravity wave. The cluster in the center of the circle represents the highly damped gravity waves, while the many eigenvalues with modulus of almost unity represent the only weakly damped Rossby waves.

APPENDIX C

Numerical Diffusion of the Upwind Scheme

The advection of temperature and salinity is formulated in an implicit upwind scheme:

$$T^t = T^{t-\tau} + \tau \sum u_i^+ (T_i^t - T^t),$$

where the summation runs over all neighboring points for which u_i is directed toward the point of computation. For the suppression of mode splitting we add an explicit diffusion of 200 m^2 s^{-1}. It can easily be shown (cf. Bacastow and Maier-Reimer 1990) that the upwind scheme can be decomposed into a sum of advective and diffusive flux divergence with diffusion coefficients $|u|\delta x$.

In a one-dimensional constant flow u, a wavelike disturbance $T^{t-\tau} = T_0 \exp(ikx)$ is modified by this scheme according to

$$T^t = T_0\{1 + (u\tau/\delta x)[1 - \cos(k\delta x) + i \sin(k\delta x)]\}^{-1} \times \exp(ikx).$$

This represents in addition to the phase shift a damping similar to that produced by a diffusivity in the order of $|u|\delta x$. Many schemes have been presented to overcome this damping. In most cases, the different schemes are intercompared for the situation of a uniformly rotating fluid. Russell and Lerner (1981), however, have shown in their presentation of the "slope" scheme that in a practical application the diffusivity of the upwind scheme appears to be less detrimental than would be concluded from such simplified tests.

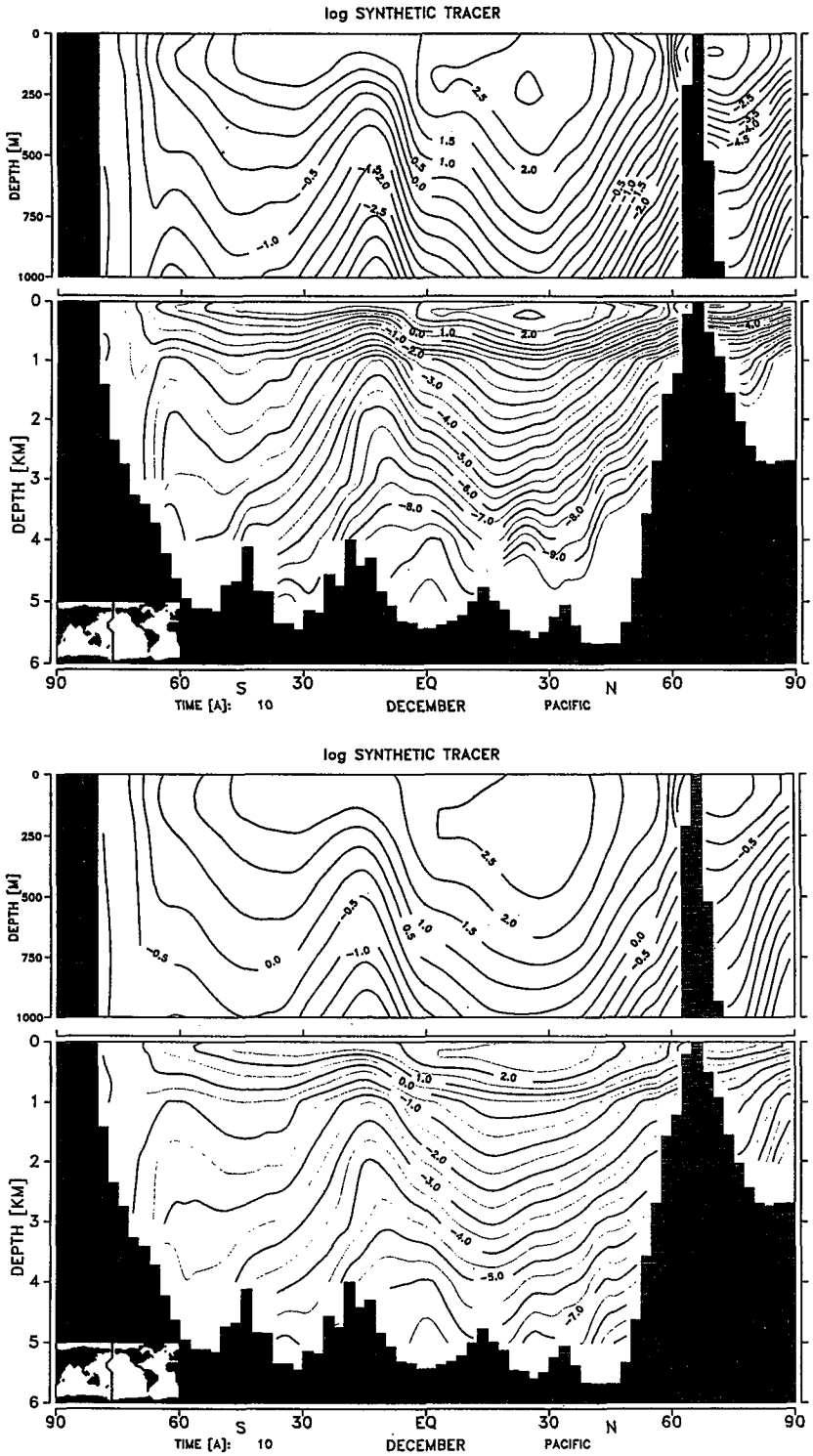

FIG. C1. Pacific sections of an artificial dye release of 10^6 units at a point off China (a: top) after 10 years with standard advection and (b: bottom) after 10 years with standard advection with doubled numerical diffusion.

To investigate the effective diffusivity in our model, we performed some simple experiments with an assumed δ-functionlike initial distribution (the worst case) of an artificial tracer.

1) The initial distribution of an artificial tracer was set at 10^6 at a point off China in both of the overlapping grids. The transport was computed in the same way as temperature and salinity in the model. This location was chosen to avoid as far as possible regions of convective mixing. The computation was performed for 10 years.

2) Experiment 1 was repeated with the amplitude of the numerical diffusive terms doubled.

3) One thousand tracer particles were distributed over an area represented by two grid points. The trajectories were computed with a 1-day time step. A diffusion coefficient of 200 $m^2 s^{-1}$ (same as the explicit diffusion in the circulation model for the suppression of mode splitting) was simulated in this run by the superposition of Brownian motion of appropriate amplitude on the advection field. This experiment with small explicit diffusivity demonstrates the effect of shear dispersion on an initial grid element.

4) Experiment 3 was repeated with an (acceptable) explicit horizontal diffusion coefficient of 10^3 $m^2 s^{-1}$ and a vertical diffusion coefficient of 10^{-4} $m^2 s^{-1}$.

Figure C1 shows Pacific sections for the experiments 1 and 2. During the 10 years of computation, the tracer is seen to remain almost entirely above the main thermocline. The doubled diffusion coefficient creates some visible but nonsubstantial additional dilution.

Figure C2 shows the time development of the horizontal and vertical variance for the four experiments. Most of the apparent diffusion of experiment 1 is clearly explained by shear diffusion, not by numerical diffusion.

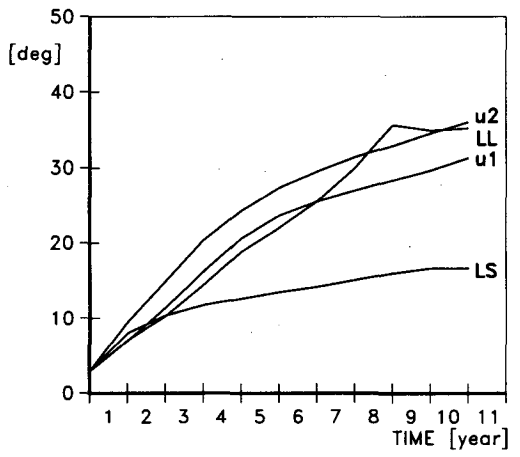

FIG. C2a. Horizontal spreading of an artificial dye release off China: (U1) standard upwind advection, (U2) upwind advection with doubled numerical diffusion, (LS) tracer particles with explicit horizontal diffusion coefficient of 200 $m^2 s^{-1}$, and (LL) tracer particles with explicit horizontal diffusion coefficient of 1000 $m^2 s^{-1}$ and a vertical diffusion coefficient of 10^{-4} $m^2 s^{-1}$.

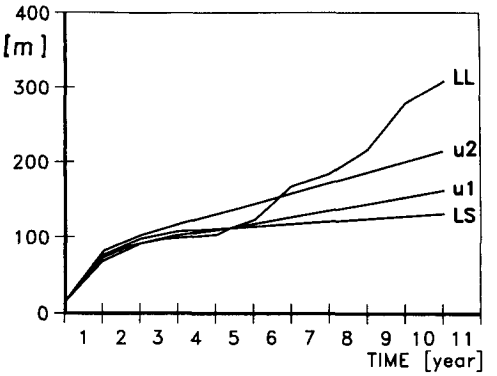

FIG. C2b. Vertical spreading of an artificial dye release off China: (U1) standard upwind advection, (U2) upwind advection with doubled numerical diffusion, (LS) tracer particles with explicit horizontal diffusion coefficient of 200 $m^2 s^{-1}$, and (LL) tracer particles with explicit horizontal diffusion coefficient of 1000 $m^2 s^{-1}$ and a vertical diffusion coefficient of 10^{-4} $m^2 s^{-1}$.

REFERENCES

Arakawa, A., and V. R. Lamb, 1977: Computational design of the basic dynamical processes of the UCLA General Circulation Model. *Methods Comput. Phys.*, **17**, 173–265.

Bacastow, R., and E. Maier-Reimer, 1990: Ocean-circulation model of the carbon cycle. *Climate Dyn.*, **4**, 95–126.

Bainbridge, A. E., 1981: GEOSECS Atlantic expedition. Vol. 2: Sections and profiles. U.S. Govt. Printing Office, Washington, D.C., Stock No. 038-000-00435-2.

Bakan, S., A. Chlond, U. Cubasch, J. Feichter, H. Graf, H. Grassl, K. Hasselmann, I. Kirchner, M. Latif, E. Roeckner, R. Sausen, U. Schlese, D. Schriever, I. Schult, U. Schumann, F. Sielmann, and W. Welke, 1991: Climate response to smoke from the burning oil wells in Kuwait. *Nature*, **351**, 367–371.

Berger, W. H., 1990: The Younger Dryas cold spell: A quest for causes. *Paleogeogr., Paleoclim., Palaeoecol*, **89**, 219–237.

——, and J. S. Killingley, 1982: The Worthington effect and the origin of the Younger Dryas. *J. Mar. Res.*, **40**(Suppl.), 27–38.

——, and R. S. Keir, 1984: Glacial–holocene changes in atmospheric CO_2 and the deep-sea record. *Climate Processes and Climate Sensitivity*. J. E. Hansen, and T. Takahashi, Eds. Amer. Geophys. Union, 337–351.

Broecker, W. S., M. Andree, W. Wolfli, H. Oeschger, G. Bonani, J. Kennet, and D. Peteet, 1988: The chronology of the last deglaciation: Implications to the cause of the Younger Dryas event. *Paleoceanogr.*, **3**, 1–19.

Bryan, K., 1969: A numerical method for the study of the circulation of the World Ocean. *J. Comput. Phys.*, **4**, 347–376.

——, 1986: High latitude salinity effects and interhemispheric thermohaline circulations. *Nature*, **305**, 301–304.

——, and L. J. Lewis, 1979: A water-mass model of the World Ocean. *J. Geophys. Res.*, **84**, 2503–2517.

Bryden, H. L., 1973: New polynomials for thermal expansion, adiabatic temperature gradient, and potential temperature gradient of sea water. *Deep-Sea Res.*, **20**, 401–408.

Chamberlin, T. C., 1906: On a possible reversal of deep-sea circulation and its influence on geologic climates. *J. Geol.*, **14**, 363–372.

Craig, H., W. S. Broecker, and D. Spencer, 1981: GEOSECS Pacific expedition. Vol. 4: Sections and profiles. U.S. Govt. Printing Office, Washington, D.C.

Cubasch, U., K. Hasselmann, H. Höck, E. Maier-Reimer, U. Mi-

kolajewicz, B. D. Santer, and R. Sausen, 1992: Time-dependent Greenhouse warming Computations with a coupled Ocean–Atmosphere model, *Clim. Dyn.*, **8**, 55–69.

Esbensen, S. K., and Y. Kushnir, 1981: The heat budget of the global ocean: An atlas based on estimates from surface marine observations. Oregon State University, Climatic Research Institute, Report No. 29, 26 pp.

Fiadeiro, M. E., 1982: Three-dimensional modeling of tracers in the deep Pacific Ocean II. Radiocarbon and the circulation. *J. Mar. Res.*, **40**, 537–550.

Gordon, A. L., 1986: Interocean exchange of thermocline water. *J. Geophys. Res.*, **91**, 5037–5046.

Hasselmann, K., 1982: An ocean model for climate variability studies. *Progress in Oceanography*, Vol. 11, Pergamon, 69–92.

Heinze, C., E. Maier-Reimer, and K. Winn, 1991: Glacial pCO_2 reduction by the World Ocean—Experiments with the Hamburg Carbon Cycle Model. *Paleoceanogr.*, **6**, 395–430.

Hellerman, S., and M. Rosenstein, 1983: Normal monthly wind stress over the World Ocean with error estimates. *J. Phys. Oceanogr.*, **13**, 1093–1104.

Jouzel, J., C. Lorius, J. R. Petit, C. Genthon, N. I. Barkov, V. M. Kotlya-kov, and V. M. Petrov, 1987: Vostok ice core: A continuous isotope temperature record over the last climatic cycle (160,000 years), *Nature*, **329**, 403–408.

Latif, M., A. Sterl, E. Maier-Reimer, and M. Junge, 1993: Climate Variability in a coupled GCM. Part 1: The tropical Pacific, *J. Climate*, **6**, 5–21.

Levitus, S., 1982: Climatological atlas of the World Ocean. NOAA Prof. Paper No. 13, 173 pp.

Maier-Reimer, E., and K. Hasselmann, 1987: Transport and storage of CO_2 in the ocean: An inorganic ocean-circulation carbon cycle model. *Climate Dyn.*, **2**, 63–90.

——, and U. Mikolajewicz, 1989: Experiments with an OGCM on the cause of the Younger Dryas. *Proc. JOA 1988*, 87–100.

——, and R. Bacastow, 1990: Modelling of geochemical tracers in the ocean. *Climate–Ocean Interaction*, M. E. Schlesinger, Ed., Kluwer Academic.

——, and U. Mikolajewicz, 1990: The Hamburg Large-Scale Geostrophic Ocean Circulation Model. Tech. Rep. Deutsch. KlimaRechenZentrum, 34 pp.

Manabe, S., and R. J. Stouffer, 1988: Two stable equilibria of a coupled ocean–atmosphere model. *J. Climate*, **1**, 841–866.

Marotzke, J., 1991: Influence of convective adjustment on the stability of the thermohaline circulation. *J. Phys. Oceanogr.*, **21**, 903–907.

——, P. Welander, and J. Willebrand, 1988: Instability and multiple steady states in a meridional-plane model of the thermohaline circulation. *Tellus*, **40A**, 162–172.

Mikolajewicz, U., and E. Maier-Reimer, 1990: Internal secular variability in an OGCM. *Climate Dyn.*, **4**, 145–156.

——, B. Santer, and E. Maier-Reimer, 1990: Ocean response to greenhouse warming. *Nature*, **345**, 589–593.

Oberhuber, J. M., 1988: An Atlas based on the COADS dataset: The budgets of heat, buoyancy, and turbulent kinetic energy at the surface of the Global Ocean. Tech. Rep. No. 15, Max-Planck-Institut für Meteorologie, 199 pp.

Olbers, D. J., M. Wenzel, and J. Willebrand, 1985: The inference of North Atlantic circulation patterns from climatological hydrographic data. *Rev. Geophys.*, **23**, 313–356.

Östlund, H. G., and M. Stuiver, 1980: GEOSECS Pacific radiocarbon. *Radiocarbon*, **22**, 25–53.

Redi, M. H., 1982: Oceanic isopycnal mixing coordinate rotation. *J. Phys. Oceanogr.*, **12**, 1154–1158.

Reid, J. L., 1986: On the total geostrophic circulation of the South Pacific Ocean: Flow patterns, tracers and transports. *Progress in Oceanography*, 16, Pergamon, 1–61.

Roemmich, D., and C. Wunsch, 1985: Two trans-Atlantic sections: Meridional circulation and heat flux in the subtropical North Atlantic Ocean. *Deep-Sea Res.*, **32**, 619–664.

Rooth, C., 1982: Hydrology and ocean circulation. *Progress in Oceanography*, Vol. 11, Pergamon, 131–149.

Russel, G. L., and J. A. Lerner, 1981: A new finite-differencing scheme for the tracer transport equation. *J. Appl. Meteor.*, **20**, 1483–1498.

Sarmiento, J. L., and K. Bryan, 1982: An ocean transport model for the North Atlantic. *J. Geophys. Res.*, **87**, 394–408.

Sarnthein, M., and R. Tiedemann, 1990: Younger Dryas-style cooling events at glacial terminations I-VI or ODP Site 658: Associated benthic δ^{13} C anomalies constrain meltwater hypothesis. *Paleoceanogr.*, **5**, 1041–1055.

Stefan, R., 1891: The theory of ice formation especially in the Arctic Ocean. *Ann. Phys. Chem.*, **42**, 269–278.

Stommel, H., 1961: Thermohaline convection with two stable regimes of flow. *Tellus*, **13**, 224–230.

Stuiver, M., and H. G. Östlund, 1980: GEOSECS Atlantic radiocarbon. *Radiocarbon*, **22**, 1–24.

Toggweiler, J. R., K. Dixon, and K. Bryan, 1989: Simulations of Radiocarbon in a Coarse-Resolution World Ocean Model. Part I: Steady-State Prebomb Distributions. *J. Geophys. Res.*, **94**(C6), 8217–8242.

UNESCO, 1981: Tenth report of the joint panel on oceanographic tables and standards. UNESCO Tech. Pap., *Mar. Sci.*, **36**, 25 pp.

Welander, P., 1986: Thermohaline effects in the ocean circulation and related simple models. *Large Scale Transport Processes in Ocean and Atmosphere*, J. Willebrand, and D. L. T. Anderson, Eds., Reidel 163–200.

Wunsch, C., D. Hu, and B. Grant, 1983: Mass, heat, salt, and nutrient fluxes in the South Pacific Ocean. *J. Phys. Oceanogr.*, **13**, 725–753.

Woodruff, S. D., R. J. Slutz, R. L. Jenne, and P. M. Steurer, 1987: A comprehensive ocean–atmosphere dataset. *Bull. Amer. Meteor. Soc.*, **68**, 1239–1250.

Wüst, G., 1933: Schichtung und zirkulation des Atlantischen Ozeans. Das Bodenwasser und die Gliederung der Atlantischen Tiefsee. *Wissenschaftliche Ergebnisse der Deutschen Atlantischen Expedition auf dem Forschungs- und Vermessungsschiff "Meteor" 1925–1927*, **6**, 106 pp.